UC San Diego
UC San Diego Previously Published Works

Title

High-Efficiency Lithium-Metal Anode Enabled by Liquefied Gas Electrolytes

Permalink

Journal

ISSN

Authors

Yang, Yangyuchen
Davies, Daniel M
Yin, Yijie
et al.

Publication Date

DOI

Peer reviewed

Article

High-Efficiency Lithium-Metal Anode Enabled by Liquefied Gas Electrolytes

Liquefied Gas Electrolytes

with Fully Coordinated Co-solvent

Avg. 99.6%

Li Coulombic Efficiency (%)

- Liquefied Gas Electrlolyte
- Ether-based Electrolyte
- Carbonate-based Electrolyte

Cycle #
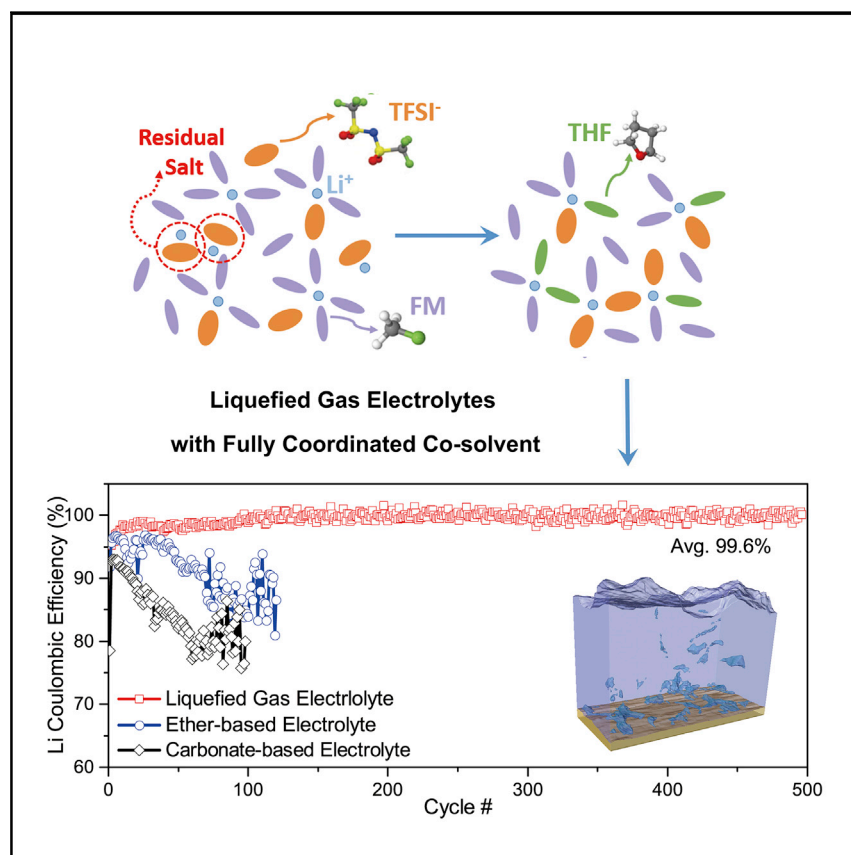
A modified liquefied gas electrolyte with the addition of fully coordinated cosolvent enables unique Li solvation structures. Their favorable properties lead to dendrite-free high Coulombic efficiency Li-metal anode cycling and enable low-temperature operation even down to $-60°C$ with high Li-metal efficiency. The system shows potential for improved energy density and low-temperature operation of Li-metal batteries.

Yangyuchen Yang, Daniel M. Davies, Yijie Yin, ..., Xuefeng Wang, Cyrus S. Rustomji, Y. Shirley Meng

oleg.a.borodin.civ@mail.mil (O.B.)
crustomji@south8technologies.com (C.S.R.)
shmeng@ucsd.edu (Y.S.M.)

HIGHLIGHTS

Unique properties and solvation structures of liquefied gas electrolytes are shown

Compact Li-metal deposition with fluorinated interfaces are demonstrated

Electrolytes enable dendrite-free cycling with outstanding Coulombic efficiency

Excellent Li-metal cyclability and rate performance are shown down to $-60°C$

Joule

Article

High-Efficiency Lithium-Metal Anode Enabled by Liquefied Gas Electrolytes

Yangyuchen Yang,[1] Daniel M. Davies,[2] Yijie Yin,[1] Oleg Borodin,[3,4,*] Jungwoo Z. Lee,[2,5] Chengcheng Fang,[1] Marco Olguin,[2] Yihui Zhang,[1] Ekaterina S. Sablina,[1] Xuefeng Wang,[2] Cyrus S. Rustomji,[5,*] and Y. Shirley Meng[1,2,6,*]

SUMMARY

Among the several challenges to enable next-generation batteries is the development of an electrolyte that maintains a dendrite-free and high Coulombic efficiency lithium-metal anode over extended cell cycling. A new electrolyte solvation structure and transport mechanism is demonstrated in fluoromethane-based liquefied gas electrolytes with the introduction of additive amounts of tetrahydrofuran, which is shown to fully coordinate with the lithium cations and greatly enhance salt dissociation and transport. The resulting electrolyte shows a high conductivity and transference number ($t_+ > 0.79$), which leads to a dramatic improvement of the cycling performance of the lithium-metal anode. Systems using the enhanced liquefied gas electrolytes demonstrate a long-term high average Coulombic efficiency of 99.6%, 99.4%, and 98.1% ($\pm$ 0.3%) at capacities of 0.5, 1, and 3 mAh·cm^{-2}, respectively, with dendrite-free morphology and remarkable rate capability. Both the rate and cycling performance are well maintained from +20°C to −60°C.

INTRODUCTION

With the highest specific capacity (3,860 mAh·g^{-1}) and the lowest electrochemical potential (−3.04 V versus SHE), the lithium (Li)-metal anode has long been considered as the "holy grail" of Li-based battery chemistry.[1–5] Nevertheless, its practical application has been hindered by numerous challenges over the past several decades, including dendrite growth, low Coulombic efficiency (CE), and large volume change.[5–8] Because of the high reactivity of Li metal, electrolytes are readily reduced and form a solid electrolyte interface (SEI) on the anode surface. Although the SEI can passivate the Li-metal surface, the inhomogeneous physical-chemical nature of the SEI often induces dendrite formation, resulting in battery failure and safety concerns. The dendrite growth also causes the formation of inactive Li during cell discharge and creates a porous Li-metal structure, which consumes both active Li and electrolyte, thus decreasing both CE and cycle life.

The nature of Li deposition and the properties of the SEI (ionic conductivity and mechanical stability) are closely correlated with the properties of the electrolyte (viscosity, ionic mobility, pressure, transport properties, etc.),[9] which are key to suppress the dendritic growth, improve CE, and enhance cycling stability of the Li-metal anode. There is currently a global effort to develop various electrolyte formulations to enable solutions that address these shortcomings of the Li-metal anode. With a relatively flexible and stable SEI, ether-based electrolytes deliver a CE of about 95%–99%, but their applications are hindered by their low oxidation stability (<4.0 V versus Li).[6,10,11] Despite their high oxidation stability (4.3 V versus Li) and

Context & Scale

The practical applications of lithium-metal batteries are hampered by incompatibilities between the lithium-metal anode and conventional electrolytes, resulting in dendrite growth and low Coulombic efficiency. With a new solvation mechanism, liquefied gas electrolytes with additive amounts of a fully coordinated cosolvent show improved salt solubility, high lithium transference numbers, and good conductivity. Because of the superior physical and chemical properties of this system, dendrite-free lithium-metal cycling with a high average Coulombic efficiency over 500 cycles of 99.6% was demonstrated. The lithium-metal cycling and rate performance is well maintained down to −60°C. Combining dendrite-free cyclability at high rates and over a wide temperature range, this study opens a promising avenue toward the applications of high-energy rechargeable lithium-metal batteries.

Joule

CellPress

successful commercialization in Li-ion batteries, carbonate-based electrolytes decompose into polymer-like SEIs that show poor compatibility with Li metal, causing low CE and dendrite growth.[12,13] Efforts were also made to form more ceramic-like SEIs by tailoring additives,[14,15] solvents,[16] salts,[17] and their ratios.[18–21] Notably, high-concentration electrolytes have been shown to minimize solvent decomposition and form LiF-rich SEIs via salt decomposition, which enables Li-metal cycling with a relatively high CE of ~99%.[18] It has also been shown that high-concentration electrolytes may also improve the oxidation stability of ether-based electrolytes by reducing free ether molecules.[19,22] Recently, the disadvantages of high-concentration electrolytes, such as high cost, high viscosity, and poor wettability, have been partially mitigated by diluting the electrolyte with non-solvating solvents to form localized high-concentration electrolytes.[21,23] However, the low-temperature performance and rate capability of the localized high-concentration electrolytes are inferior even to conventional electrolytes. Lastly, a newly developed electrolyte composed of 1 M LiPF$_6$ in a mixture of all-fluorinated ether and carbonate solvents shows excellent stability with Li metal (CE > 99%),[16] which highlights the positive contribution of fluorinated electrolytes to SEI formation.

The recently developed fluoromethane (CH$_3$F, FM)-based liquefied gas electrolyte enables dendrite-free Li-metal cycling with relatively high efficiency (97.5%) by forming a dense, uniform, ceramic-based SEI layer, composed primarily of LiF and Li$_2$CO$_3$.[24] As demonstrated in this earlier work, the solvent itself, rather than the salt, plays a more critical role in stabilizing the Li metal. Additionally, the low melting point and low viscosity of these electrolytes enable low-temperature operation as low as −60°C. However, cell performance in this previously reported work was limited by the low salt solubility and the correspondingly high polarizations. In the present study, the limited salt solubility and high polarizations are resolved by introducing tetrahydrofuran (THF) as a cosolvent. The solvation structure and improved Li transport of the electrolyte are more thoroughly understood through a combination of experimental and computational techniques. Additionally, thorough analyses of the Li-metal morphology and structure of the SEI are carried out to understand the excellent stability, CE, rate capability, and low-temperature performance achieved by the new liquefied gas system with the Li-metal anode.

RESULTS AND DISCUSSION

Physical-Chemical Properties of Liquefied Gas Electrolytes

While previous work focused on an electrolyte composition of 0.2 M bis(trifluoromethane)sulfonimide (LiTFSI) in FM,[24] more recent optical observations using high-pressure glass window cells show that less than 0.1 M LiTFSI is soluble in pure FM (Figure 1A), so several possible methods were explored to increase the solubility of the salt. It was found that THF is miscible with FM and the addition of this cosolvent (2.4 vol %) with a salt-to-THF molar ratio of 1:1 increases the Li-salt solubility considerably (Figure 1A). By controlling the 1:1 salt-to-additive molar ratio, THF is thought to be fully coordinated with Li cations, as illustrated in Figure 1B. Similar to high-concentration electrolyte systems, the fully coordinated THF solvation structure is expected to suppress the oxidation of this additive.[19,22,25]

Electrolytic conductivity measurements of the modified liquefied gas electrolytes were carried out. As detailed previously,[24] the conductivity versus temperature curves of the liquefied gas electrolytes do not follow that of typical electrolytes. Because of the exceptionally low melting point (T$_m$ = −142°C), minimal viscosity

[1]Materials Science and Engineering, University of California San Diego, La Jolla, CA 92121, USA

[2]Department of Nano Engineering, University of California San Diego, La Jolla, CA 92121, USA

[3]Electrochemistry Branch, Sensors and Electron Devices Directorate, U.S. Army Research Laboratory, Adelphi, MD 20783, USA
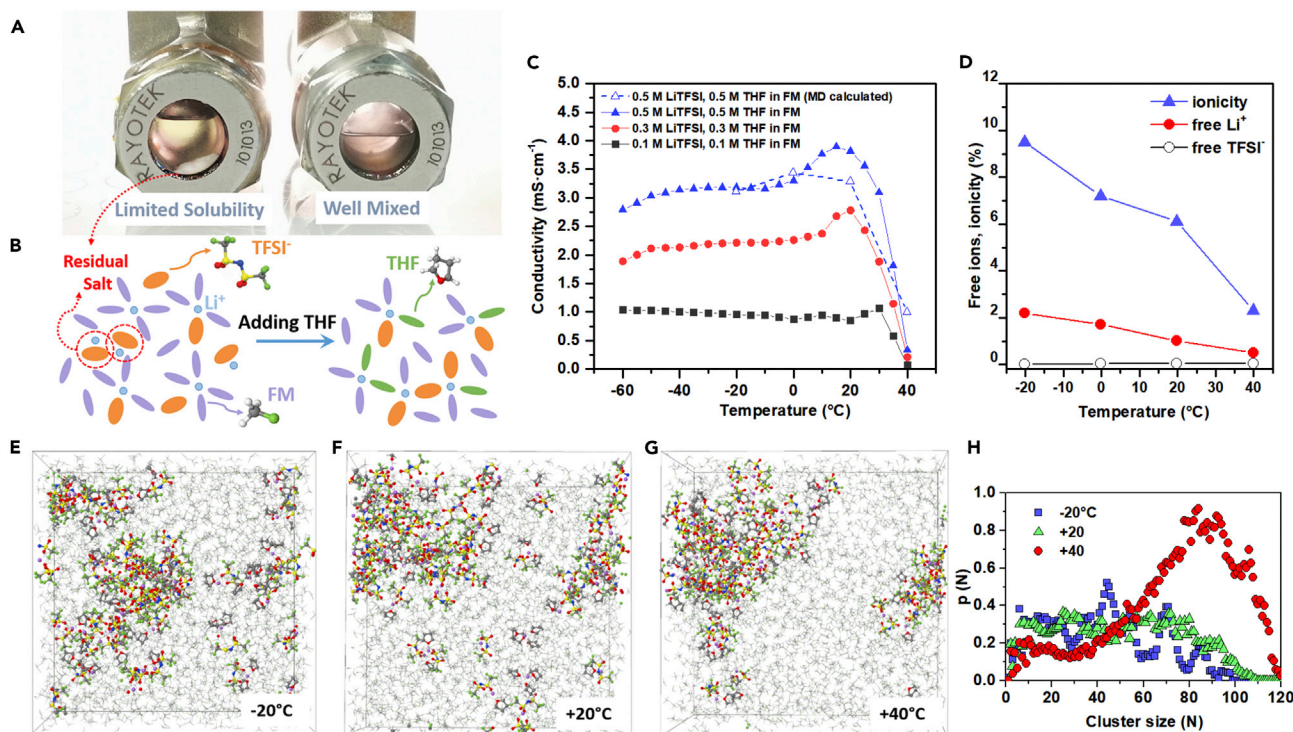
[4]Joint Center for Energy Storage Research, U.S. Army Research Laboratory, Adelphi, MD 20783, USA

[5]South 8 Technologies, Inc., San Diego, CA 92109, USA

[6]Lead Contact

*Correspondence:
oleg.a.borodin.civ@mail.mil (O.B.),
crustomji@south8technologies.com (C.S.R.),
shmeng@ucsd.edu (Y.S.M.)

https://doi.org/10.1016/j.joule.2019.06.008

Joule

CellPress

Figure 1. Properties of Liquefied Gas Electrolytes

(A) Photographs of solubility tests in window cells of 0.1 M LiTFSI in FM (left) and 0.3 M LiTFSI and 0.3 M THF in FM (right). (B) Schematic illustration of the solvation mechanism of the liquefied gas electrolyte with the THF additive. (C) Electrolytic conductivity measurements of liquefied gas electrolytes over a range of temperatures with different salt and additive concentrations and MD predicted values for 0.5 M LiTFSI and 0.5 M THF in FM. (D) Calculated fraction of free ions and degree of ion uncorrelated motion (ionicity) from MD simulations. (E–G) Snapshots of the MD simulation cell containing liquefied gas electrolyte (0.5 M LiTFSI, 0.5 M THF in FM) at −20 (E), +20 (F), and +40 (G)°C. Color: Li, purple; O, red; C, gray; H, white; N, blue; S, yellow; and F, green. (H) Probability of the ion to be a part of an ionic cluster with size N corresponding to electrolytes shown in (E–G).

(η = 0.085 mPa·s), and high dielectric-fluidity factor ($\varepsilon_r \cdot \eta^{-1}$ = 114 (mPa·s)$^{-1}$) of FM, the conductivity is well maintained at low temperatures. Notably, the conductivity is substantially enhanced with an increase in concentration of the salt and additive while the conductivity still follows the same temperature trends as the FM-based electrolyte without the addition of THF. The electrolytic conductivity of 0.5 M LiTFSI and 0.5 M THF in FM shows a maximum conductivity of 3.9 mS·cm^{-1} at +20°C. An impressive low-temperature conductivity of 2.8 mS·cm^{-1} is achieved at −60°C, which is substantially higher than previously reported (1.1 mS·cm^{-1})[24] and compares favorably with some state-of-the-art low-temperature electrolytes.[26,27] Because of the decreasing dielectric constant and precipitation of salt out of the electrolyte as the temperature approaches the critical point of FM ($T_{c, FM}$ = +44°C), the conductivity shows a sudden drop.[24] Similar electrolytic conductivity phenomena are observed with the introduction of THF (Figure 1C), which indicates that the salt still strongly aggregates at increased temperatures despite the improved solubility with the addition of THF. Strategies to enable an increased operating temperature at commercially acceptable temperatures have been demonstrated and will be published in future work.

In order to obtain further insight into the solvation structure and the Li$^+$ transport mechanisms of the modified liquefied gas electrolytes, molecular dynamics (MD) simulations were performed with the focus on the most conductive concentration of 0.5 M LiTFSI and 0.5 M THF in FM. Predicted conductivity from MD simulations

agrees well with the experimental value as shown in Figure 1C. A drop in conductivity as temperature increases to $+40°$ C is attributed to the decrease of ionicity (degree of ion uncorrelated motion) to ca. 2% as shown in Figure 1D. This is attributed to a drop in the fraction of free Li ions below 0.5%. Further analysis of the ion solvation shell indicates that at all simulated temperatures no free $TFSI^-$ ions are observed, while the fraction of free Li^+ uncoordinated by $TFSI^-$ anions increases approximately linearly with decreasing temperature. Snapshots from MD simulations (Figures 1E–1G) indicate that at $+40°C$ most ions aggregate, forming essentially one large cluster with an occasional free Li^+ cation and a few smaller aggregates. Figure 1H quantitatively confirms that at $+40°C$ most ions belong to large aggregate clusters with a peak at 90 ions out of 128 total number of ions in the simulation cell. The formation of smaller clusters and a subsequent increase in the fraction of free lithium ions is observed as temperature drops to $+20°C$ and below, thus compensating for the slight decrease of ion self-diffusion coefficients shown in Figure S1. This results in the approximately constant conductivity over a wide temperature range from $-20°C$ to $+20°C$. Despite similar average self-diffusion coefficients for Li^+ and $TFSI^-$, the diffusion of the free Li^+ is 2–2.5 times faster than the average diffusion coefficients of all Li^+ and $TFSI^-$ anions as shown in Figure S2. The much higher fraction of free Li^+ as compared to free $TFSI^-$ indicates a high contribution of Li^+ to the electrolytic conductivity compared to anion contribution that move slower and essentially do not exist as free ions. The Li transference number (t_+) is calculated using the Onsager reciprocal relations combined with a linear response theory as yielding $t_+ > 0.95$ (Figure S3C), which is supported by the measured Li^+ transference number as high as $t_+ = 0.79$ (Figure S4). High ionic correlations are responsible for the increased t_+ compared to the transport number based upon self-diffusion coefficients that yield only 0.5 as shown in Figures S3A and S3B.

Analysis of the Li^+ solvates yields 0.98–1.02 THF, 2.09–2.22 TFSI anions, and 0.4–0.67 CH_3F coordinating to each Li^+ on average. Interestingly, THF is not uniformly distributed among free Li^+ and Li^+ participating in aggregates. Free Li^+ tends to be primarily coordinated by 2, 3, or 4 THF molecules with 2, 1, or 0 FM, respectively, as shown in Figures S5 and S6, with the $Li^+(THF)_3FM$ solvate being the most frequently observed. Thus, free Li^+ are surrounded preferentially by THF while the Li^+ participating in aggregates have fewer coordinating THF on average, clarifying the role of THF in salt dissociation.

Li-Metal Cycling Performance

The cycling and rate performances of Li-metal plating and stripping in liquefied gas electrolytes were examined on polished stainless-steel electrodes. As discussed previously,[24] the addition of 5 wt % CO_2 to the fluoromethane-based liquefied gas electrolyte helps stabilize the Li-metal anode and is similarly used in the present study. At a current density of 0.5 mA·cm^{-2}, an overpotential of 13 mV is observed, which is comparable to that of the carbonate-based electrolyte, 1 M $LiPF_6$ in ethylene carbonate:diethyl carbonate (EC:DEC 1:1), and the ether-based electrolyte, 1 M LiTFSI, 2 wt % $LiNO_3$ in 1,3-dioxolane:1,2-dimethoxyethane (DOL:DME 1:1), and improved from a similar liquefied gas electrolyte without the THF additive (Figure 2A). Liquefied gas electrolytes with THF additives significantly improved the Li-metal cycling stability and CE. All CE efficiencies reported have an uncertainty of ± 0.3%, as described in the Experimental Procedures. As shown in Figure 2B, at 0.5 mA·cm^{-2}, the CE ramps up from an initial value of 93.6% to an average CE of 98.6% during the first 100 cycles. An impressive average CE of 99.9% is achieved from the 100th to 500th cycle, demonstrating an overall average CE of 99.6% (± 0.3%) over all 500 cycles. It is thought that a stable interface is formed during

Joule

CellPress
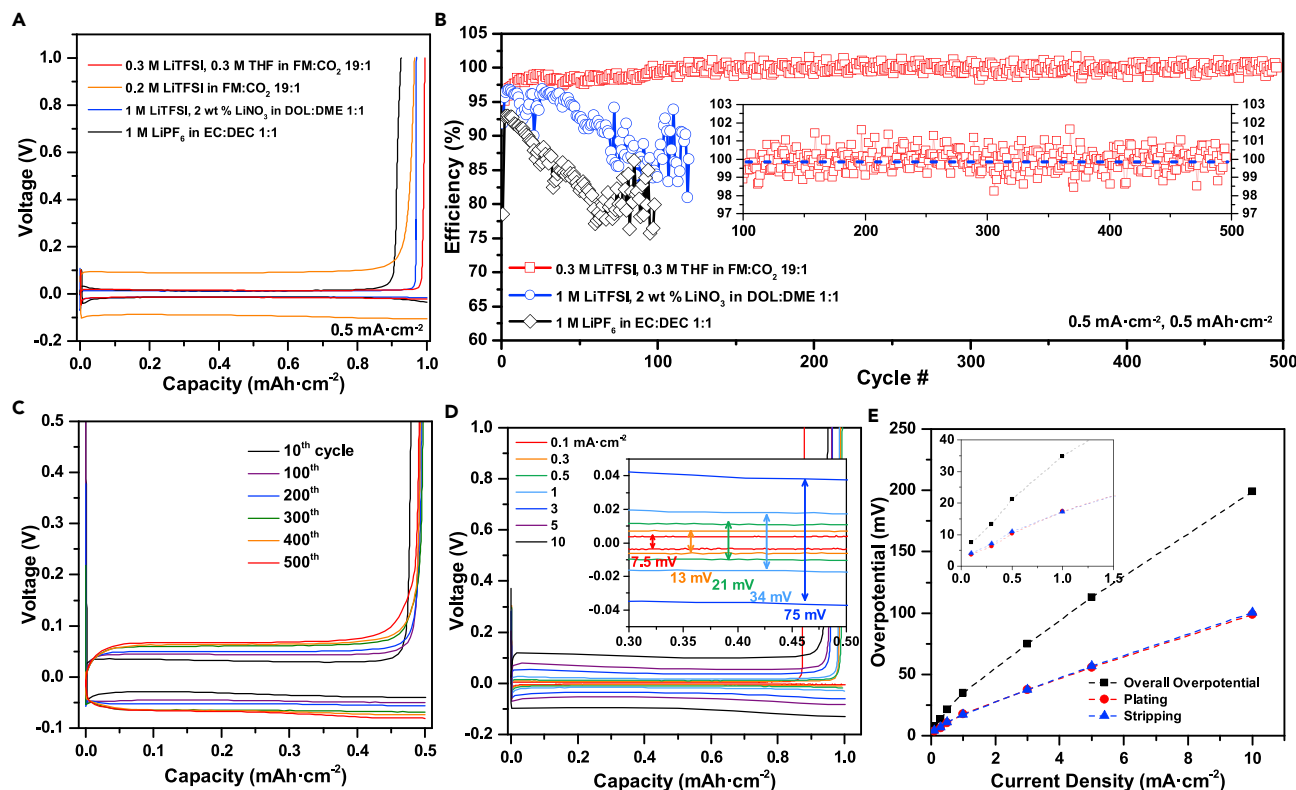
Figure 2. Electrochemical Performance of Li-Metal Plating and Stripping in Liquefied Gas Electrolyte

(A) Voltage profiles of the 20th cycle of Li-metal plating and stripping. (B) The CE of Li plating and stripping over 500 cycles. (C) Voltage profiles for the cell using the liquefied gas electrolyte used in (B). Polarization profiles (D) and quantitative summary (E) for Li plating and stripping at various current densities.

the first ca. 100 cycles, after which more stable cycling is observed via the increase in CE. CE slightly above 100% is observed regularly. It is hypothesized that a small portion of electrically disconnected metallic Li formed within the SEI of previous cycles electrically reconnects to the metallic bulk structure in a future cycle, which accounts for the CE occasionally being over 100%. This is likely due to the breaking of a relatively brittle SEI layer by temperature and volume change during cycling. A similar phenomenon has also been observed in other dendrite-free electrolytes.[16,20] The voltage profile also remains stable with a slight increase in overpotential (Figure 2C). For comparison, carbonate-based and ether-based electrolytes demonstrate unstable CE with averages of ca. 85% and 95%, respectively (Figure 2B). At an increased Li cycling capacity of 1 mAh·cm^{-2} at the same current density, the CE in the liquefied gas electrolyte remains at 99.4% for 200 cycles with less CE fluctuation after 20 initial activation cycles (Figure S7). At an increased current density and capacity of 1 mA·cm^{-2} and of 1 mAh·cm^{-2}, respectively, an average CE of 98.7% is achieved after initial activation from cycles 100–900 with a similarly stable overpotential throughout cycling (Figure S8). The electrochemical performance of the liquefied gas electrolyte is also impressive at high rates up to 10 mA·cm^{-2} with a stable voltage profile (Figure 2D). The polarization of the liquefied gas electrolyte increases nearly linearly and symmetrically with the current density, reaching 100 mV at 10 mA·cm^{-2} (Figures 2D and 2E). The nearly linear polarization is indicative of the highly ionically conducting Li-metal SEI layer and high ion diffusion through the electrolyte. Combined with the high CE, this high rate performance is substantially superior in comparison to the carbonate-based electrolyte,

Joule

CellPress

ether-based electrolyte (Figure S9), all-fluorinated electrolyte,[16] high-concentration electrolyte,[20] and localized high-concentration electrolyte systems[21] (Figure S10).

In order to ascertain the commercial viability of the use of these electrolytes, we also demonstrate successful cycling of a $Li_4Ti_5O_{12}$-$LiNi_{0.8}Co_{0.15}Al_{0.05}O_2$ (LTO/NCA) jelly roll (0.8 Ah, 1.3–2.7 V, and 4.2 V versus Li) in a conventional 18650 form factor with a custom cell cap to enable liquefied gas electrolyte injection and solvent containment under pressurized conditions (Figure S11). Although manufacturing challenges remain, the demonstration of a conventional 18650 form factor to safely contain the electrolyte under pressurized conditions reduces barriers to commercialize practical devices.

Low-Temperature Performance

The low-temperature operation is a large challenge for Li-ion batteries, resulting from a reduced electrolytic conductivity, an increase in SEI impedance, and a limited Li-ion diffusivity within the electrodes.[28] Contrary to intercalated anodes, such as graphite,[29] the hostless feature of the Li-metal anode removes the necessity for long distance charge transfer in the host, which is a substantial benefit of the Li-metal anode for low-temperature applications. Because of the unique nature of liquefied gas electrolytes, the low melting point and high dielectric-fluidity factors enable excellent conductivity down to $-60°C$. Therefore, the low-temperature performance of the Li-metal anode with the liquefied gas electrolyte was further explored.

Extended cycling of Li metal at various temperatures was compared in the liquified gas, carbonate-based, and ether-based electrolyte systems (Figure 3A). At $+20°C$, the CE of the carbonate-based electrolyte is limited to ca. 90% and at $-20°C$ shows a continuous drop in CE (ca. 78%) with a considerable increase in overpotential. The cell fails to cycle at lower temperatures and shows reduced performance when warmed to room temperature (Figure 3B). In the ether-based electrolyte, the CE fading at low temperature is even worse, and the cell fails to cycle when warmed back to room temperature. In contrast, the CE of the liquified gas electrolyte increases to 99.5% within 20 cycles at $+20°C$, and an average CE of 98.6% with stable polarization is observed at $-20°C$. The cell cycles equally well at lower temperatures, demonstrating a stable CE of 98.4% at $-60°C$ with an average overpotential of 0.28 V. When brought back to $+20°C$, the voltage profile of the cell perfectly matches that of the initial state (Figure S12), with a CE marginally higher than 100%, indicating recovery of dead Li formed at lower temperatures, which is likely due to the restructuring and volume expansion of the surface layer during the temperature increase.

The voltage profiles for Li-metal rate tests at various temperatures are shown for both the liquefied gas electrolyte (Figure 3C) and the carbonate-based electrolyte (Figure S13). The liquefied gas electrolyte demonstrates highly stable Li-metal cycling with remarkable capacity retention down to $-40°C$ at 10 $mA \cdot cm^{-2}$ and even down to $-60°C$ at 5 $mA \cdot cm^{-2}$ (Figure 3C), while the overpotential increases irregularly for 10 $mA \cdot cm^{-2}$ cycling at $-60°C$. As summarized in Figure 3D, the polarization linearly increases with current at temperatures down to $-40°C$, which suggests the impedance is dominated by ohmic resistance and the electrolyte is not diffusion limited even at such low temperatures. The carbonate-based electrolyte in contrast is only stable at low platting and stripping currents (<0.5 $mA \cdot cm^{-2}$) and shows unstable cycling with a substantial increase in overpotential at higher current densities at $-20°C$ (Figure S13). Estimated from Tafel plots (Figure S14), the exchange current densities (Table S1) show the fast kinetics of the liquefied gas electrolyte and its interfaces at different temperatures, which are 1.4, 6.5, and
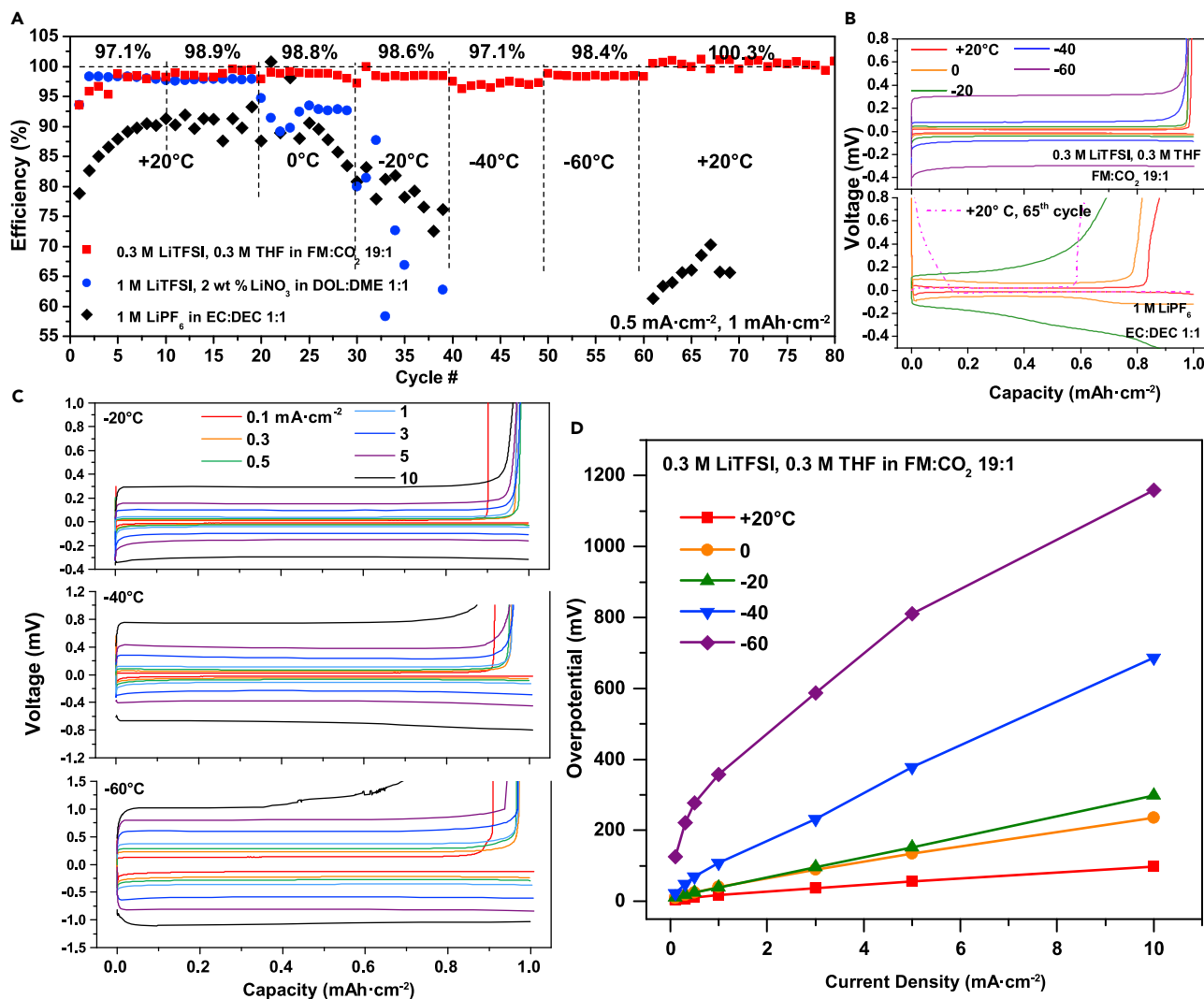
Figure 3. Li-Metal Low-Temperature Electrochemical Performance in Liquefied Gas Electrolyte

(A) The CE of Li plating and stripping at various temperatures. (B) Voltage profiles for the cells cycled in (A). (C) Li-metal plating and stripping voltage profiles at various currents and temperatures. (D) Average overpotential summary of the liquefied gas electrolyte.

14.9 times higher than that of the carbonate-based electrolyte at +20°C, 0°C, and −20°C, respectively.

Li-Metal Morphology

The surface and cross-sectional morphology of Li-metal deposition in the liquefied gas electrolyte was observed via scanning electron microscopic (SEM) and cryogenic-focused ion beam (cryo-FIB). Cryogenic techniques have proven useful for preserving and probing morphological and chemical phenomena of Li metal, and recently cryo-FIB has been demonstrated to quantitatively characterize bulk morphology of electrochemically deposited Li and enable transmission electron microscopy (TEM) analysis of Li-metal/electrolyte interfaces.[30–33] Li metal is extremely reactive at room temperature because of its low melting temperature, density, thermal conductivity, and shear modulus, making samples prone to deleterious cascade effects and Ga-ion implantation during FIB milling, resulting in morphological and chemical artifacts. To overcome this challenge, cryo-FIB was

Joule

CellPress
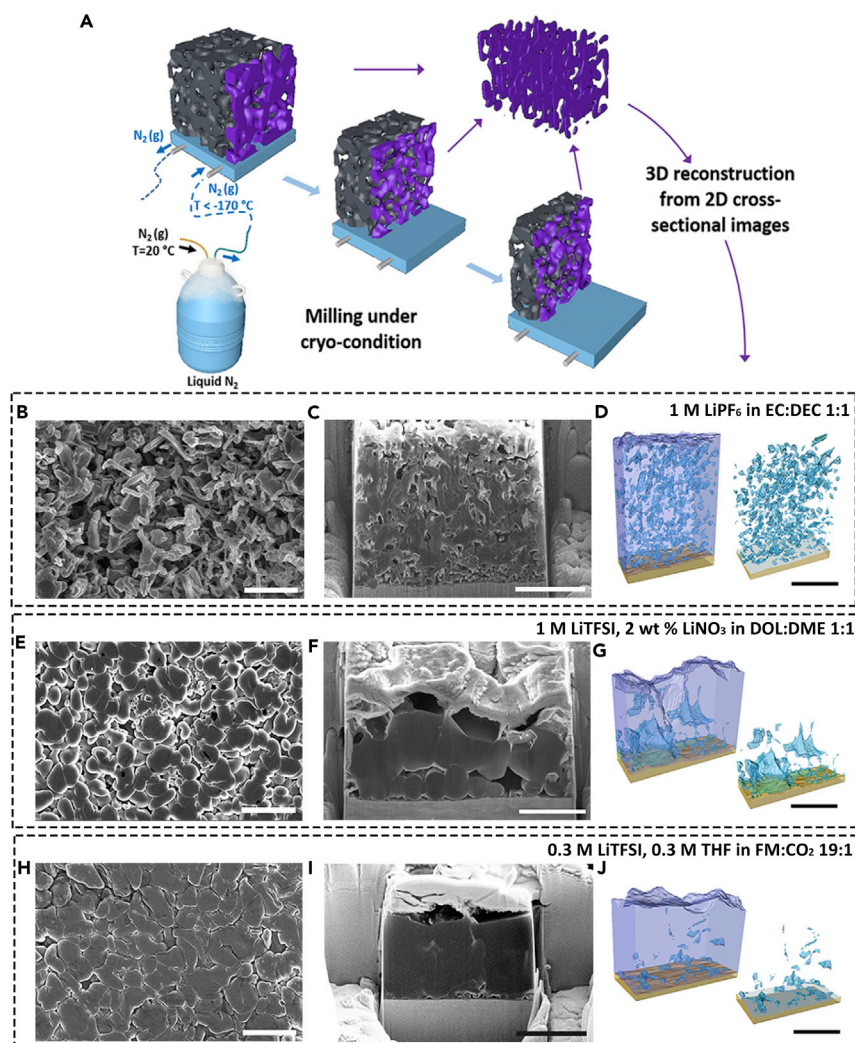
Figure 4. Cryo-FIB Characterization of the Morphologies of Electrochemically Deposited Li and its 3D Reconstruction

(A) Schematic illustration for cryo-FIB and 3D reconstruction processes. (B–J) Images show morphologies of electrochemically plated Li metal in 1 M $LiPF_6$ in EC:DEC 1:1 (B–D), 1 M LiTFSI, 2 wt % $LiNO_3$ in DOL:DME 1:1 (E–G), and 0.3 M LiTFSI, 0.3 M THF in $FM:CO_2$ 19:1 (H and I), at a current density of 0.5 mA·cm^{-2} with a capacity of 1 mAh·cm^{-2} for one cycle on a SS316L working electrode. Top-view SEM images (B, E, and H) have a scale bar of 10 μm; cross-sectional SEM images (C, F, and I) have a scale bar of 3 μm; and 3D reconstruction models (D, G, and J) contrast voids (blue) and bulk Li metal (purple) of the electrochemically deposited Li with scale bar of 5 μm.

applied to minimize damage when preparing Li cross-sections for SEM imaging and 3D reconstruction to explore the bulk microstructure of the deposited Li metal (Figures 4A and S15). Samples were plated with a capacity of 1 mAh·cm^{-2} at 0.5 mA·cm^{-2} on a stainless-steel electrode, which corresponds to a theoretical thickness of ~5 μm for perfectly dense Li.

As shown in Figure 4B, the Li deposited in carbonate-based electrolyte generates needle-like dendrites with numerous pores. The cross-sectional observations reveal the Li-metal film as having a porous structure and large voids present at both the Li/substrate interface and the bulk structure of the deposited Li, resulting in a total thickness of >10 μm (Figures 4C and S16). The 3D reconstructed model of deposited

Joule

CellPress

Table 1. Physical Properties of the Bulk Structure of Plated Li in Different Electrolytes

Electrolyte	1 M LiPF$_6$ in EC:DEC	1 M LiTFSI, 2 wt % LiNO$_3$ in DOL:DME	0.3 M LiTFSI, 0.3M THF in FM:CO$_2$ 19:1
Ideal thickness (μm)	5	5	5
Real thickness (μm)	10.1	5.5	5.3
Particle shape	needle like	grain like	grain like
Particle size	~100 nm	1–7 μm	3–7 μm
Porosity (%)	16.8	8.2	0.90
Normalized void surface area (μm^{-1})	1.32	0.82	0.096
1st cycle CE (%)	86.7	91.9	93.6

The qualitative and quantitative data are summarized from cryo-FIB-SEM observations and 3D reconstructions. The normalized void surface area (μm^{-1}) is defined as the void surface area (μm^2) per unit volume (μm^3).

Li metal in the carbonate-based electrolyte illustrates that large void spaces (16.8%) are present through the entire bulk and the interface (Figure 4D), causing a large normalized void surface area of 1.32 μm^{-1} (Table 1). The ether-based electrolyte enables a dendrite-free Li deposition with roundly shaped Li particles (Figure 4E). However, the cross-sectional view shows that large voids are generated on the Li/substrate interface (Figures 4F and S17), which is further elucidated in the 3D reconstruction that shows a relatively large porosity of 8.2% (Figures 4G and S18; Table 1). In contrast, the liquefied gas electrolyte presents densely packed, large, roundly shaped Li particles forming a smooth dendrite-free surface (Figures 4H and S16). From the cross-sectional view, the liquefied gas electrolyte forms a very dense Li deposition with a thickness of 5.3 μm (Figures 4I and S17). At an increased 3 mAh·cm^{-2} capacity of deposited Li, the compact bulk structure is well maintained with a thickness of 15.5 μm (Figure S19). The 3D reconstructed model of deposited Li metal in the liquefied gas electrolyte shows a much denser deposition with minimal porosity (0.90%) and normalized void surface area (0.096 μm^{-1}) (Figures 4J and S18; Table 1). The deposited Li-metal morphology after 20 cycles for all tested electrolytes is consistent with the initial plating (Figures S20 and S21). Additionally, the large particle size and compacted morphology in the liquefied gas electrolyte is maintained even after 100 cycles (Figure S22). On the stripping side, the liquefied gas electrolyte enables a thinner and denser layer of sheet-like residue, revealing minimal formation of dead Li. In summary, unlike the dendrite formation in the carbonate-based electrolyte or the large voids at Li/substrate in the ether-based electrolyte, the liquefied gas electrolyte shows a densely packed deposition of Li that allows for excellent structural connection with low porosity, increasing the CE, limiting the volume change, and limiting the increase in polarization during long-term cycling.

Chemistry at the Interphase

The impedance of the electrolyte and the Li-metal SEI layer at various temperatures were investigated by electrochemical impedance spectroscopy (EIS) (Figures 5A–5C). The x axis intercept in the high-frequency region corresponds to the bulk electrolyte resistance R$_e$, and the following semicircle is assigned to the interfacial resistance (R$_{int}$ = R$_{int1}$ + R$_{int2}$) from the electrodes. In both carbonate and ether-based electrolytes, R$_e$ exhibits a 5x enlargement when the temperature is reduced to −40°C while the liquefied gas electrolyte shows good low-temperature compatibility with only a 20% increase in R$_e$ down to −60°C (Figure 5C; Table S2), which is in the agreement with the previous electrolyte conductivity measurements (Figure 1C). Nevertheless, it is known that the SEI often contributes to a higher
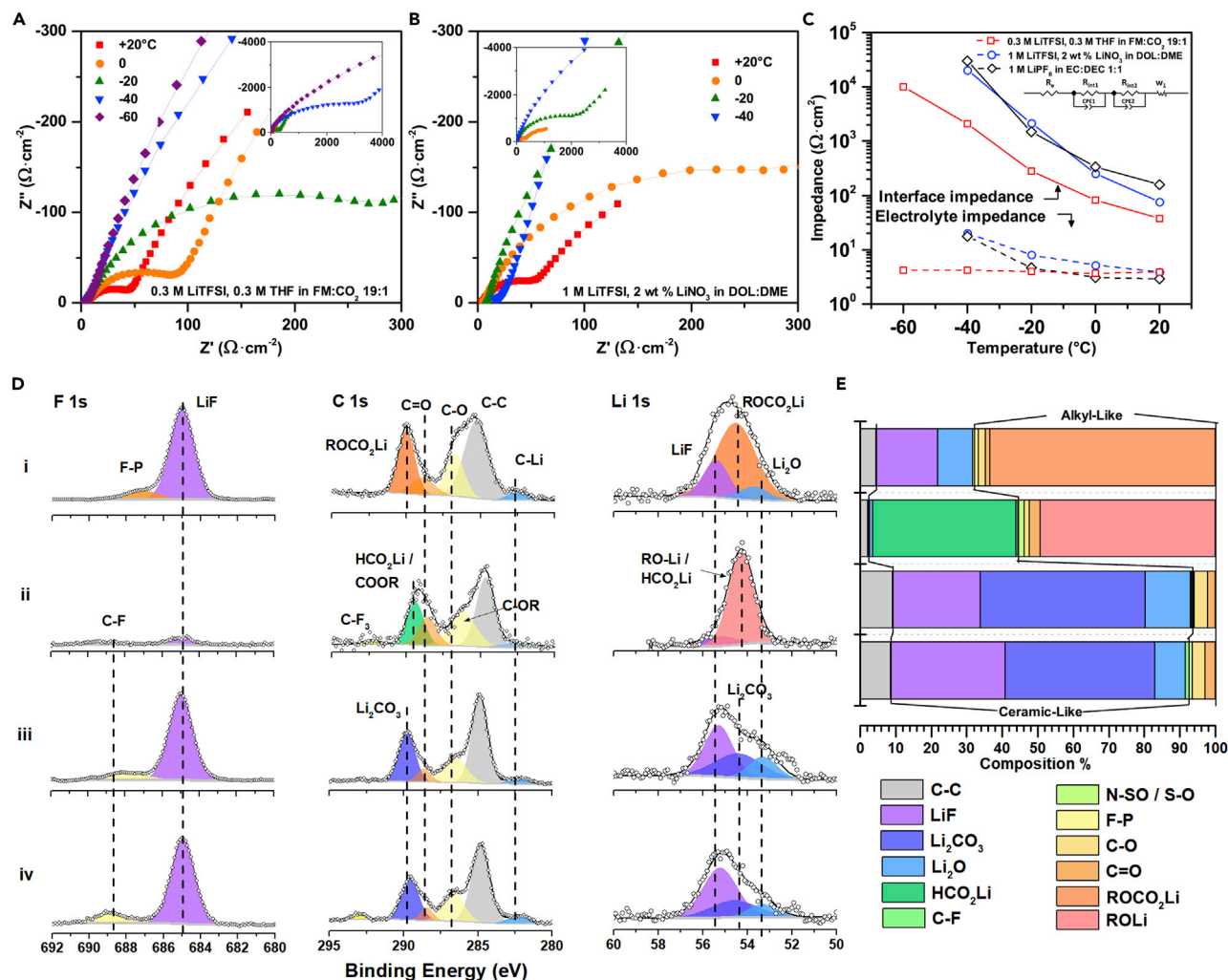
Figure 5. Impedance and Chemical Characterization of the Lithium Metal Interface

(A–C) Electrochemical impedance spectra of (A) 0.3 M LiTFSI, 0.3 M THF in FM:CO_2 19:1; (B) 1 M LiTFSI, 2 wt % $LiNO_3$ in DOL:DME 1:1, at various temperatures; and (C) their fitting analysis. (D and E) XPS chemical analysis (D) of the Li-metal interface using (i) 1 M $LiPF_6$ in EC:DEC 1:1, (ii) 1 M LiTFSI, 2 wt % $LiNO_3$ in DOL:DME 1:1, (iii) 0.2 M LiTFSI in FM:CO_2 19:1, (iv) 0.3 M LiTFSI, 0.3 M THF in FM:CO_2 19:1, and the percent composition calculations (E) of the Li-metal interface.

impedance compared to that of the electrolyte at low temperatures.[28] As summarized in Figure 5C, the SEI layer is the dominant component of the impedance in all these systems as temperature increases. At all measured temperatures, the R_{int} of the liquefied gas electrolyte is roughly an order of magnitude less than that of the carbonate and ether-based electrolyte, which indicates that a dense and highly ionically conductive SEI is present in the liquefied gas electrolyte system.

Insights into the composition and formation mechanism of the SEI in liquefied gas electrolytes can be obtained from the X-ray photoelectron spectroscopy (XPS) on the cycled Li-metal electrode (Figures 5D and S23). The differences in the SEI components and formation mechanisms between conventional liquid electrolytes and liquefied gas electrolytes are pronounced. For the carbonate-based electrolyte (Figure 5Di, 1 M $LiPF_6$ in EC:DEC 1:1), the SEI formed is dominated by Li alkyl carbonates ($ROCO_2Li$) with a heterogeneous distribution of inorganic LiF from

$LiPF_6$ decomposition. This results in a poorly ionically conducting and unstable SEI.[10,34] The ether-based electrolyte (Figure 5Dii, 1 M LiTFSI, 2 wt % $LiNO_3$ in DOL:DME 1:1) is able to partially passivate Li-metal surface by forming mainly inorganic components such as Li formate (HCO_2Li) and organic species such as $-(CH_2CH_2O)_n$- and short chain oligomers with $-OLi$ edge groups (ROLi).[10,35] The relatively small S 2p and N 1s spectra (Figure S23) confirm that the low fluorine concentration in the SEI (Figure 5D, F 1s) is caused by the limited decomposition of LiTFSI. In contrast, a highly fluorinated ceramic-like SEI is formed in the liquefied gas electrolyte without addition of THF (Figure 5Diii, 0.2 M LiTFSI in FM:CO_2 19:1). Although the LiTFSI decomposition is still limited (Figure S23, S 2p, N 1s), the main components of the solvent, fluoromethane, and carbon dioxide, reduce to LiF and Li_2CO_3, respectively, components that previous computational studies have shown combine synergistically to enhance ionic conductivity.[36] Importantly, there is no notable change in the SEI chemical composition with, (Figure 5Div) and without, (Figure 5Diii) the addition of THF for all spectra. Together with no obvious change in C-O band (Figures 5D and 5E), this indicates that there is little to no decomposition of THF. There is a slight increase in the S 2p and N 1s spectra, suggesting a larger (but still small) amount of LiTFSI may be involved in the SEI formation due to improved solubility. It is also supported by the enlargement of the ratio of LiF, which may contribute to improve the ionic conductivity of the SEI layer[20,37] (Figure 5E). In agreement with previous studies showing benefits of a highly fluorinated interface,[38] both the fluoromethane solvent and salt in the present study are rich sources of fluorine and contribute to the large presence of LiF in the SEI. The additional Li_2CO_3 component found in the Li-metal SEI from carbon dioxide reduction is thought to combine with the LiF to provide an overall positive impact on the overall electrochemical performance.[36]

Conclusions

Combining superior physical and chemical properties, liquefied gas electrolytes have high compatibility with the Li-metal anode, showing excellent CE at high rates and over a wide temperature range. The introduction of THF as a cosolvent, which coordinates with the Li cations, increases salt dissociation and transport, ionic conductivity, and addresses the solubility and polarization issues previously seen with the liquefied gas electrolytes. The use of the fluoromethane-based liquefied gas electrolyte yields a dense and uniform Li-metal deposition and stable and dendrite-free Li-metal cycling with a high average CE over 500 cycles of 99.6%, with remarkable rate performance up to 10 mA·cm^{-2}. The Li-metal cycling and rate performance is well maintained down to $-60°C$ because of the high dielectric-fluidity factor and exceptional electrolytic conductivity at low temperatures with a low-impedance SEI. Combining dendrite-free cyclability at high rates and over a wide temperature range, as well as demonstration of the compatibility of the electrolyte with conventional form factors, the liquefied gas electrolyte chemistry provides a promising path toward high-energy Li-metal chemistries.

EXPERIMENTAL PROCEDURES

Materials

Fluoromethane (99.99%) was obtained from Air Liquide. The salts Li hexafluorophosphate ($LiPF_6$) (99.9%) and Li bis(trifluoromethane)sulfonamide (LiTFSI) (99.9%) were purchased from BASF. 1M $LiPF_6$ in EC: DEC 1:1 (LP40) was purchased from BASF. Tetrahydrofuran (THF, anhydrous, 99.9%), 1,2-dimethoxyethane (DME, 99.5%), and 1,3-dioxolane (DOL, 99.8%) were purchased from Sigma-Aldrich and stored over molecular sieves.

Joule

Electrochemical Measurements

Electrolytic conductivity measurements were carried out in a custom-fabricated high-pressure stainless-steel cell, in which polished stainless steel (SS316L) were used as both electrodes. The cell constant was calibrated from 0.447 to 80 mS·cm^{-1} using OAKTON standard conductivity solutions.

EIS measurements were conducted with a sinusoidal probe voltage of 5 mV from 0.1 Hz to 1 MHz in the same cell setup. The impedance of Li plating and stripping cells were measured after 20 cycles (1 and 0.5 mAh·cm^{-2}). The spectra were fitted by an equivalent circuit model using ZView software.

Battery cycling performance was evaluated by an Arbin battery test station (BT2043, Arbin Instruments, USA) in custom designed coin cells, with Li metal (FMC Li, 1 mm thickness, $\frac{1}{4}$ inch diameter) as the counter electrode and polished SS316L as the working electrode. A single 20 μm porous polypropylene separator (Celgard 2075) was used for all the electrochemical experiments.

For Li-metal plating and stripping experiments, Li was first deposited onto the working electrode at 0.5 mA·cm^{-2} until 0 V versus Li and the voltage was held for 5 h to form a stable SEI on the current collector, the capacity of which is around 0.02–0.04 mAh·cm^{-2} and is also accounted for in the first cycle efficiency. The first plating cycle was then started, followed by complete Li stripping to a 1 V versus Li cut off voltage. For one-time deposition, a total charge of 1 mAh·cm^{-2} was transferred at a current density of 0.5 mA·cm^{-2}. The current collector with deposited Li was taken from the glovebox for further characterization and analysis. For long-term Li-metal cycling, the cells were cycled at a specific current density and capacity, with a cutoff potential of 1 V versus Li for Li stripping under the same current density. The CE was calculated as the Li stripping capacity divided by the Li plating capacity during a single cycle. For the rate and temperature tests, the cell was placed in a temperature chamber (Espec), soaked at the testing temperature for several hours, then cycled with capacity of 1 mAh·cm^{-2} for 3 cycles at each selected current density (from 0.1 to 10 mA·cm^{-2}) at each selected temperature (from +20 to −60°C), respectively.

CE uncertainty was calculated by finding the error in current measurement from the Arbin using a current equivalent to that used in Li plating and stripping experiments (0.5 mA/cm^2). Current measurements were made through a calibrated ammeter and a shunt resistor in series with the Arbin. Errors on several Arbin channels were measured. When describing the uncertainty in the measurements, we report the largest error seen among the channels tested. These come out to be a 0.30% underestimation, and a 0.29% overestimation of the measured efficiency—which are rounded to measurement uncertainties of ± 0.3%.

Room temperature cycling of the 18650 form factor cells with the liquefied gas was performed in conventional 18650 nickel-plated steel cans (0.25 mm wall thickness) using a custom designed cell cap to enable liquefied gas electrolyte injection and contain the pressurized electrolyte.

Electrolyte Addition

Electrolyte addition procedures have been described previously.[24]

Material Characterization

SEM images were collected with a Zeiss Sigma 500 field-emission equipped with ultrahigh resolution (UHR) mode operating at 5 kV and 0.1 nA.

Joule

CellPress

Cryogenic-focused ion beam (cryo-FIB) (FEI Scios DualBeam equipped with a CryoMat integrated cryo-stage and air-free quick loader) was applied to explore the morphology of the cross-section and bulk structure of electrochemically deposited Li. To reduce curtaining artifacts during milling, the samples were coated with organometallic platinum at room temperature using a gas injection system. To minimize the beam damage, at high vacuum ($\sim 10^{-6}$ mbar) the samples are cooled down to $-170°C$ and maintained under a continuous chilled nitrogen gas cooling during SEM imaging and FIB operation. To prepare cross-sectional images, samples were rough milled with a cross-sectional cut (30 kV and 5 nA) followed by a cross-sectional cleaning cut (30 kV and 0.5 nA). To explore the 3D bulk structure, cross-sectional images were sequentially collected while continuously milling through a large sample area. Using Amira-Avizo software these images were segmented to generate a 3D reconstruction model for quantitative analysis.

XPS was performed using a Kratos AXIS Supra DLD XPS with monochromatized Al Kα radiation ($\lambda = 0.83$ nm and $h\upsilon = 1486.7$ eV) under a base pressure of $<10^{-8}$ Pa. To avoid moisture and air exposure, samples were transferred to the XPS chamber directly from a glovebox via vacuum transfer. All spectra were calibrated with hydrocarbon C 1s (284.6 eV) and analyzed by CasaXPS software. The surface is also cleaned by 30s Ar^+ sputtering under 10k eV.

To remove residual salt on the surface, all samples were slightly rinsed with DMC and dried in a glovebox antechamber before analysis.

Computational Methods

MD simulations were performed using an APPLE&P polarizable force field.[39,40] The LiTFSI force field parameters from previous work were used.[39] The Li^+/THF and Li^+/FM parameters were developed in this work following previously described methodology by fitting to quantum chemistry (QC) data.[41] Partial charges were fit to reproduce electrostatic potential around the solvents and solvent/Li^+ complexes calculated using the Møller-Plesset perturbation theory (MP2) with aug-cc-pvTz basis set. The dihedral parameters for THF were fit to reproduce molecular deformation energy that was also calculated at the MP2/aug-cc-pvTz level. Binding energy for the $Li^+(FM)_4$ complex was 344 kJ/mol from molecular mechanics (MM) calculations using force field parameters, which is slightly lower than predictions from the G4MP2 hybrid QC methodology of 353 kJ/mol. Binding energy of $Li^+(THF)$ was 173 kJ/mol from both MM calculations using the developed force field and G4MP2 QC calculations indicating an accurate description of the Li^+ binding to FM and THF by the developed force field.

MD simulation cells contained 64 LiTFSI, 64 THF, and 2,163 FM molecules corresponding to the experimentally investigated electrolyte composition for 0.5 M LiTFSI and 0.5 M THF in FM at room temperature. Two replicas were created by randomly removing 77 FM molecules from the equilibrated system comprised of 64 LiTFSI, 64 THF, and 2,240 FM molecules that were simulated for 60–90 ns at $-20°C$, $0°C$, $+20°C$, and $+40°C$. Simulations were performed in constant volume-temperature (NVT) ensemble using Nose-Hover thermostat. Equilibration runs were 40–112 ns followed by 70–131 ns production runs as shown in Table S3 for all simulated systems. Multiple timestep integration was employed with a timestep of 0.5 fs for bonded interactions, 1.5 fs for all nonbonded interactions within a truncation distance of 8.0 Å, and an outer timestep of 3.0 fs for all nonbonded interactions between 8.0 Å and the nonbonded truncation distance of 18 Å. Because of the high aggregation and non-homogeneous distribution of salt and solvent, a very large cutoff distance of 18 Å for dispersion and real space of electrostatic

Joule

CellPress

interactions was adopted. The Ewald summation method was used for the electrostatic interactions between permanent charges with permanent charges or induced dipole moments with $k = 7^3$ vectors. The reciprocal part of Ewald was calculated every 3.0 fs. Induced dipoles were found self-consistently with convergence criteria of 10^{-9} (electron charge * Å)^2. Additional simulation details and methodology used for calculation of transport properties is given in the Supplemental Information. The MD source code and input files are attached in a separate zip file (Data S1).

SUPPLEMENTAL INFORMATION

Supplemental Information can be found online at https://doi.org/10.1016/j.joule.2019.06.008.

AUTHOR CONTRIBUTIONS

Y. Yang, C.S.R., and Y.S.M. conceived the idea and designed the experiments. Y. Yang, Y. Yin, D.M.D., and C.S.R. conducted the solubility tests, conductivity tests, and electrochemical performance experiments. O.B. carried out the MD simulations and developed the force field. M.O., D.M.D., and J.Z.L. provided electrolyte compositions for MD simulations. J.Z.L. set up cryo-FIB instrumentation and helped Y. Yang to perform the characterization. Y. Yang, C.F., and X.W. conducted the interface characterizations. Y.Z. and E.S.S. helped on the control experiments. Y. Yang, D.M.D., O.B., and C.S.R. prepared the manuscript with input from X.W. and other co-authors. All authors have given approval to the final version of the manuscript.

DECLARATION OF INTERESTS

Patent applications relating to this work include PCT/US14/066015, PCT/US17/29821, PCT/US2019/032414, and PCT/US2019/032413. Y.S.M. is a member of the scientific advisory board for South 8 Technologies.

Joule

CellPress

REFERENCES

1. Whittingham, M.S. (1976). Electrical energy storage and intercalation chemistry. Science *192*, 1126–1127.

2. Armand, M., and Tarascon, J.M. (2008). Building better batteries. Nature *451*, 652–657.

3. Chu, S., and Majumdar, A. (2012). Opportunities and challenges for a sustainable energy future. Nature *488*, 294–303.

4. Choi, J.W., and Aurbach, D. (2016). Promise and reality of post-lithium-ion batteries with high energy densities. Nat. Rev. Mater *1*, 16013.

5. Lin, D., Liu, Y., and Cui, Y. (2017). Reviving the lithium metal anode for high-energy batteries. Nat. Nanotechnol *12*, 194–206.

6. Xu, K. (2004). Nonaqueous liquid electrolytes for lithium-based rechargeable batteries. Chem. Rev. *104*, 4303–4418.

7. Goodenough, J.B., and Kim, Y. (2010). Challenges for rechargeable Li batteries †. Chem. Mater *22*, 587–603.

8. Xu, W., Wang, J., Ding, F., Chen, X., Nasybulin, E., Zhang, Y., and Zhang, J. (2014). Lithium metal anodes for rechargeable batteries. Energy Environ. Sci. *7*, 513–537.

9. Cheng, X.-B., Zhang, R., Zhao, C.-Z., and Zhang, Q. (2017). Toward safe lithium metal anode in rechargeable batteries: a review. Chem. Rev. *117*, 10403–10473.

10. Aurbach, D. (2000). Review of selected electrode–solution interactions which determine the performance of Li and Li ion batteries. J. Power Sources *89*, 206–218.

11. Gofer, Y., Ben-Zion, M., and Aurbach, D. (1992). Solutions of LiAsF6 in 1, 3-dioxolane for secondary lithium batteries. J. Power Sources *39*, 163–178.

12. Ding, F., Xu, W., Chen, X., Zhang, J., Engelhard, M.H., Zhang, Y., Johnson, B.R., Crum, J.V., Blake, T.A., Liu, X., et al. (2013). Effects of carbonate solvents and lithium salts on morphology and coulombic efficiency of lithium electrode. J. Electrochem. Soc. *160*, A1894–A1901.

13. Huff, L.A., Tavassol, H., Esbenshade, J.L., Xing, W., Chiang, Y., and Gewirth, A.A. (2016). Identification of Li-Ion battery SEI compounds through 7Li and 13C solid-state MAS NMR spectroscopy and MALDI-TOF mass spectrometry. ACS Appl. Mater. Interfaces *8*, 371–380.

14. Ding, F., Xu, W., Graff, G.L., Zhang, J., Sushko, M.L., Chen, X., Shao, Y., Engelhard, M.H., Nie, Z., Xiao, J., et al. (2013). Dendrite-free lithium deposition via self-healing electrostatic shield mechanism. J. Am. Chem. Soc. *135*, 4450–4456.

15. Markevich, E., Salitra, G., and Aurbach, D. (2017). Fluoroethylene carbonate as an important component for the formation of an effective solid electrolyte interphase on anodes and cathodes for advanced Li-ion batteries. ACS Energy Lett. *2*, 1337–1345.

16. Fan, X., Chen, L., Borodin, O., Ji, X., Chen, J., Hou, S., Deng, T., Zheng, J., Yang, C., Liou, S., et al. (2018). Non-flammable electrolyte enables Li-metal batteries with aggressive cathode chemistries. Nat. Nanotechnol. *13*.

17. Miao, R., Yang, J., Feng, X., Jia, H., Wang, J., and Nuli, Y. (2014). Novel dual-salts electrolyte solution for dendrite-free lithium-metal based rechargeable batteries with high cycle reversibility. J. Power Sources *271*, 291–297.

18. Qian, J., Henderson, W.A., Xu, W., Bhattacharya, P., Engelhard, M., Borodin, O., and Zhang, J. (2015). High rate and stable cycling of lithium metal anode. Nat. Commun *6*, 6362.

19. Jiao, S., Ren, X., Cao, R., Engelhard, M.H., Liu, Y., Hu, D., Mei, D., Zheng, J., Zhao, W., Li, Q., et al. (2018). Stable cycling of high-voltage lithium metal batteries in ether electrolytes. Nat. Energy *3*, 739–746.

20. Fan, X., Chen, L., Ji, X., Deng, T., Hou, S., Chen, J., Zheng, J., Wang, F., Jiang, J., Xu, K., et al. (2018). Highly fluorinated interphases enable high-voltage Li-metal batteries. Chem *4*, 174–185.

21. Chen, S., Zheng, J., Yu, L., Ren, X., Engelhard, M.H., Niu, C., Lee, H., Xu, W., Xiao, J., Liu, J., et al. (2018). High-efficiency lithium metal batteries with fire-retardant electrolytes. Joule *2*, 1548–1558.

22. Alvarado, J., Schroeder, M.A., Zhang, M., Borodin, O., Gobrogge, E., Olguin, M., Ding, M.S., Gobet, M., Greenbaum, S., Meng, Y.S., et al. (2018). A carbonate-free, sulfone-based electrolyte for high-voltage Li-ion batteries. Mater. Today *21*, 341–353.

23. Ren, X., Chen, S., Lee, H., Mei, D., Engelhard, M.H., Burton, S.D., Zhao, W., Zheng, J., Li, Q., Ding, M.S., et al. (2018). Localized high-concentration sulfone electrolytes for high-efficiency lithium-metal batteries. Chem *4*, 1877–1892.

24. Rustomji, C.S., et al. (2017). Liquefied gas electrolytes for electrochemical energy storage devices. Science, eaal4263.

25. Wang, J., Yamada, Y., Sodeyama, K., Chiang, C.H., Tateyama, Y., and Yamada, A. (2016). Superconcentrated electrolytes for a high-voltage lithium-ion battery. Nat. Commun *7*, 12032.

26. Smart, M.C., Ratnakumar, B.V., and Surampudi, S. (2002). Use of organic esters as cosolvents in electrolytes for lithium-ion batteries with improved low temperature performance. J. Electrochem. Soc. *149*, A361–A370.

27. Dong, X., Guo, Z., Guo, Z., Wang, Y., and Xia, Y. (2018). Organic batteries operated at −70°C. Joule *2*, 902–913.

28. Zhang, S.S., Xu, K., and Jow, T.R. (2004). Electrochemical impedance study on the low temperature of Li-ion batteries. Electrochim. Acta *49*, 1057–1061.

29. Zhang, S.S., Xu, K., and Jow, T.R. (2002). Low temperature performance of graphite electrode in Li-ion cells. Electrochim. Acta *48*, 241–246.

30. Li, Y., Li, Y., Pei, A., Yan, K., Sun, Y., Wu, C., Joubert, L., Chin, R., Koh, A.L., Yu, Y., et al. (2017). Atomic structure of sensitive battery materials and interfaces revealed by cryo–electron microscopy. Science *358*, 506–510.

31. Wang, X., Zhang, M., Alvarado, J., Wang, S., Sina, M., Lu, B., Bouwer, J., Xu, W., Xiao, J., Zhang, J., et al. (2017). New insights on the structure of electrochemically deposited lithium metal and its solid electrolyte interphases via cryogenic TEM. Nano Lett. *17*, 7606–7612.

32. Zachman, M.J., Tu, Z., Choudhury, S., Archer, L.A., and Kourkoutis, L.F. (2018). Cryo-STEM mapping of solid–liquid interfaces and dendrites in lithium-metal batteries. Nature *560*, 345–349.

33. Lee, J.Z., Wynn, T.A., Schroeder, M.A., Alvarado, J., Wang, X., Xu, K.Y., and Meng, S. (2018). Cryogenic focused ion beam for characterization of lithium metal anodes for next generation lithium metal batteries. ACS Energy Lett., (under review).

34. Aurbach, D., Ein-Ely, Y., and Zaban, A. (1994). The surface chemistry of lithium electrodes in alkyl carbonate solutions. J. Electrochem. Soc. *141*, L1–L3.

35. Aurbach, D., Pollak, E., Elazari, R., Salitra, G., Kelley, C.S., and Affinito, J. (2009). On the surface chemical aspects of very high energy density, rechargeable Li–sulfur batteries. J. Electrochem. Soc. *156*, A694–A702.

36. Zhang, Q., Pan, J., Lu, P., Liu, Z., Verbrugge, M.W., Sheldon, B.W., Cheng, Y., Qi, Y., and Xiao, X. (2016). Synergetic effects of inorganic components in solid electrolyte interphase on high cycle efficiency of lithium ion batteries. Nano Lett. *16*, 2011–2016.

37. Gunceler, D., Letchworth-Weaver, K., Sundararaman, R., Schwarz, K.A., and Arias, T.A. (2013). The importance of nonlinear fluid response in joint density-functional theory studies of battery systems. Modelling Simul. Mater. Sci. Eng. *21*.

38. Wang, C., Meng, Y.S., and Xu, K. (2019). Perspective—Fluorinating interphases. J. Electrochem. Soc. *166*, A5184–A5186.

39. Borodin, O. (2009). Polarizable force field development and molecular dynamics simulations of ionic liquids. J. Phys. Chem. B *113*, 11463–11478.

40. Suo, L., Borodin, O., Gao, T., Olguin, M., Ho, J., Fan, X., Luo, C., Wang, C., and Xu, K. (2015). "Water-in-salt" electrolyte enables high-voltage aqueous lithium-ion chemistries. Science *350*, 938–943.

41. Borodin, O., Giffin, G.A., Moretti, A., Haskins, J.B., Lawson, J.W., Henderson, W.A., and Passerini, S. (2018). Insights into the structure and transport of the lithium, sodium, magnesium, and zinc bis(trifluoromethansulfonyl)imide salts in ionic liquids, and zinc bis(trifluoromethansulfonyl) imide salts in ionic liquids. J. Phys. Chem. C *122*, 20108–20121.
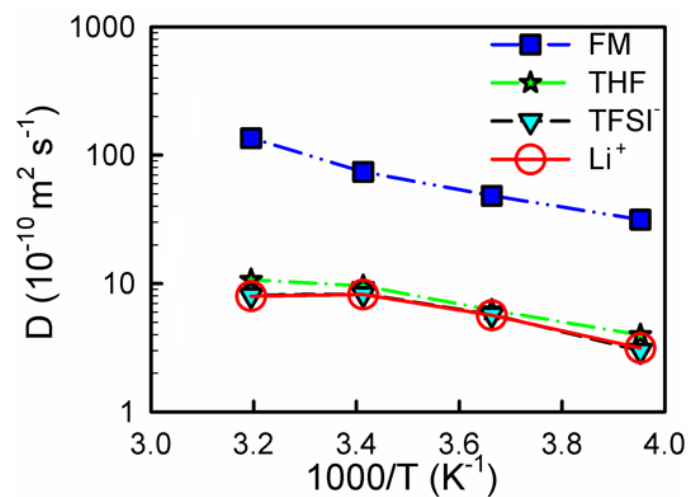
Supplemental Information

High-Efficiency Lithium-Metal Anode

Enabled by Liquefied Gas Electrolytes

Yangyuchen Yang, Daniel M. Davies, Yijie Yin, Oleg Borodin, Jungwoo Z. Lee, Chengcheng Fang, Marco Olguin, Yihui Zhang, Ekaterina S. Sablina, Xuefeng Wang, Cyrus S. Rustomji, and Y. Shirley Meng

Figure S1. Self-diffusion coefficients from MD simulations of 0.5 M LiTFSI, 0.5 M THF in FM. THF, TFSI$^-$ and Li$^+$ self-diffusion coefficients are very similar over the whole simulated temperature range.
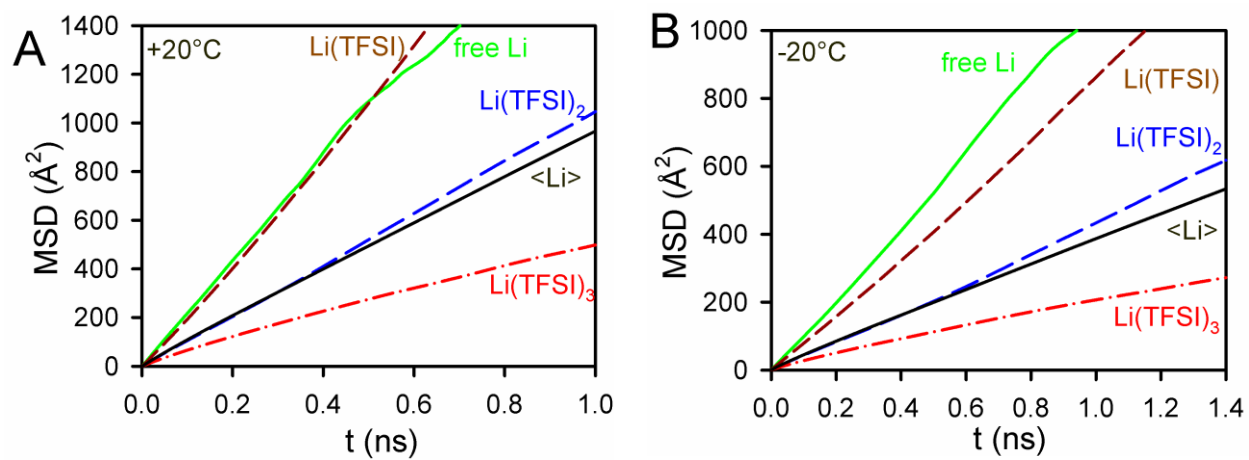
Figure S2. Mean-square displacements (MSD) of the free Li^+ cations and Li^+ cations that are coordinated by 1,2 or 3 $TFSI^-$ anions with the distance between Li^+ and $N(TFSI^-) < 5$ Å from MD simulations of 0.5 M LiTFSI, 0.5 M THF in FM. Average diffusion coefficient over all lithiums is labeled as <Li>.
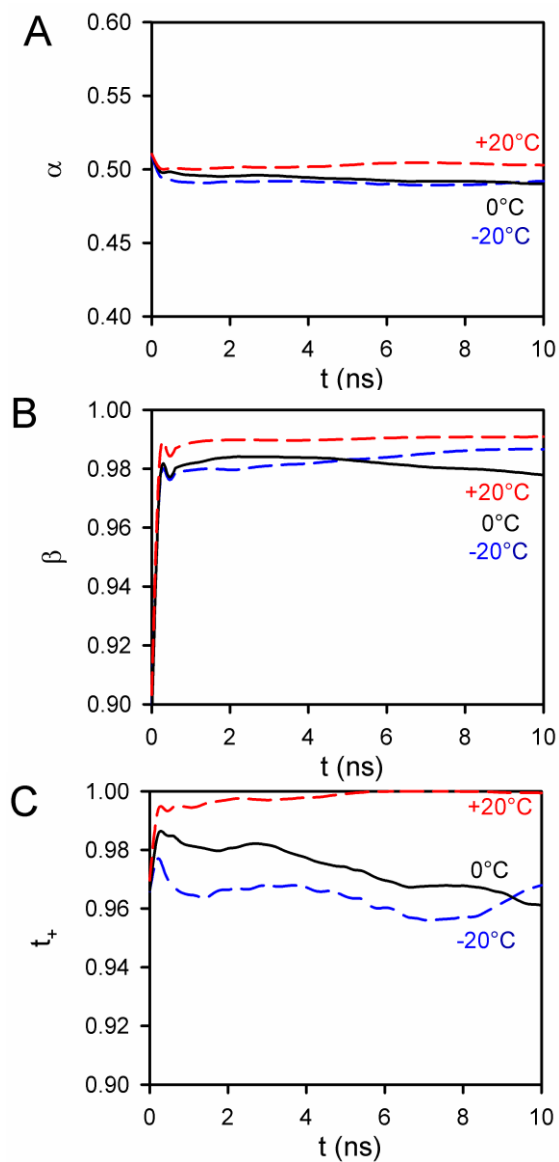
Figure S3. Representative behavior of α coefficient (A), β coefficient (B) and the apparent transference number t_+ (C) extracted from MD simulations of 0.5 M LiTFSI, 0.5 M THF in FM. The Li^+ cation transference number (t_+) was estimated from MD simulations using formalism proposed by Roling group[1] with the apparent t_+ values indicating that most of the charge transfer (>0.95) is attributed to Li^+. See discussion below in SI in the Notes on Extracting Transport Properties from Molecular Dynamics Simulations Section.
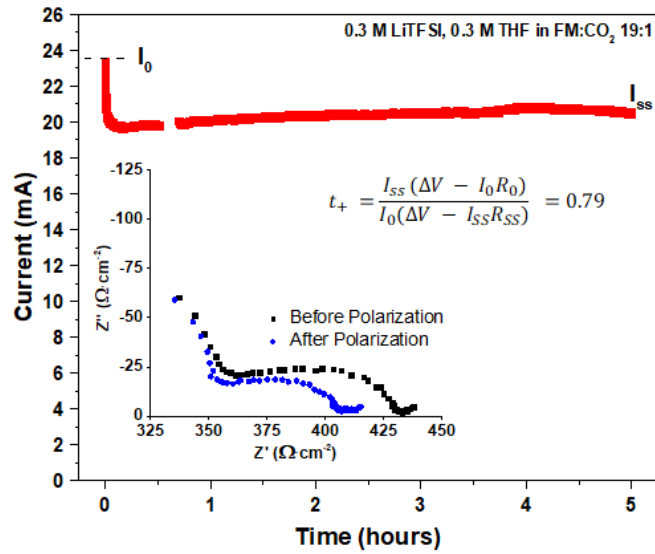
Figure S4. Polarization curve of the cell with liquefied gas electrolyte with an applied voltage of 10 mV. I_0 indicates the initial current, I_{ss} indicates the steady state current.

The transference number is measured by the potentiostatic polarization method[2]. For conventional carbonate electrolyte, using an identical method, a transference number for the cation t_+ of 0.34 is calculated by[2]:

$$t_+ = \frac{I_{ss}(\Delta V - I_0 R_0)}{I_0(\Delta V - I_{SS}R_{SS})}$$
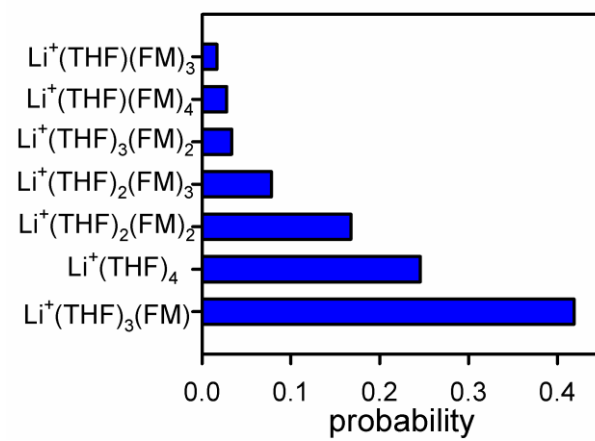
Figure S5. Populations of the Li$^+$ solvation shell at +20°C from MD simulation of 0.5 M LiTFSI, 0.5 M THF in FM.
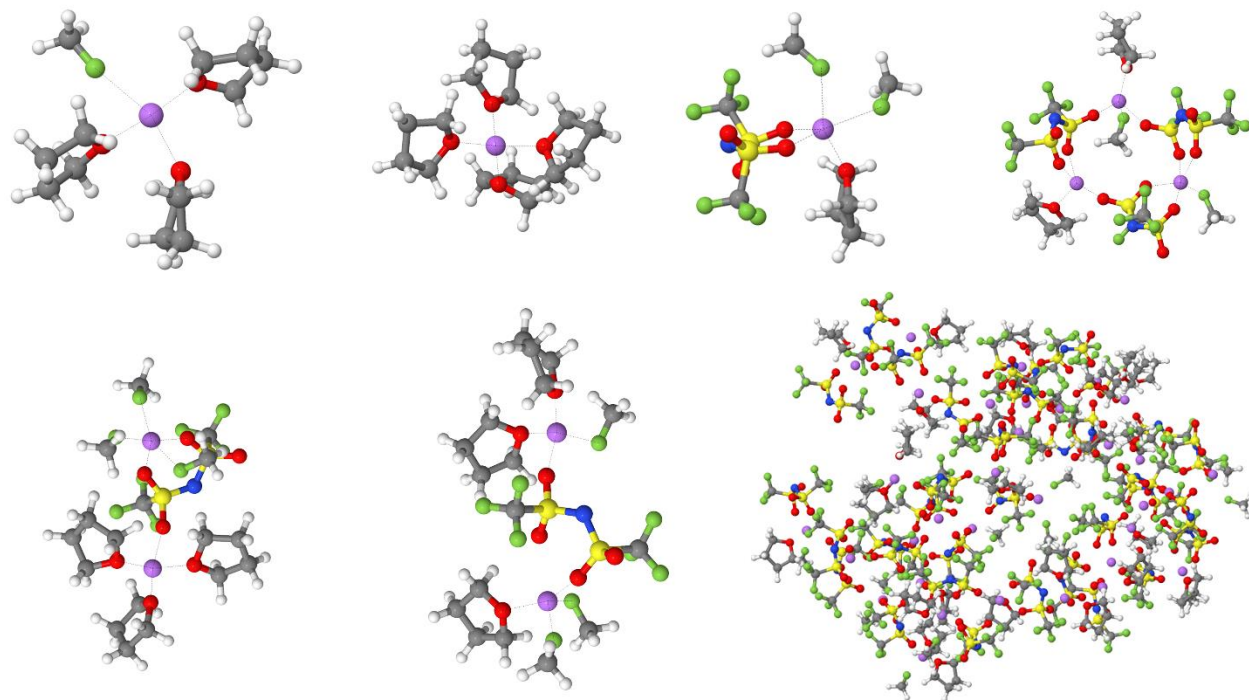
Figure S6. The Li$^+$ solvates observed in MD simulations of 0.5 M LiTFSI, 0.5 M THF in FM at +20°C.
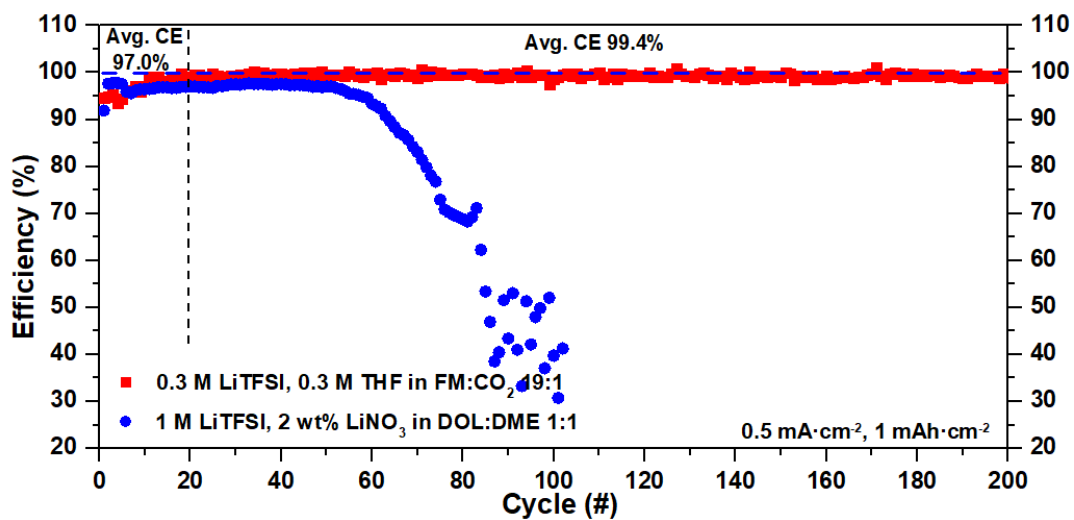
Figure S7. Electrochemical performance of Li-metal plating and stripping at a current density of 0.5 mA·cm^{-2}, with a capacity of 1 mAh·cm^{-2}.
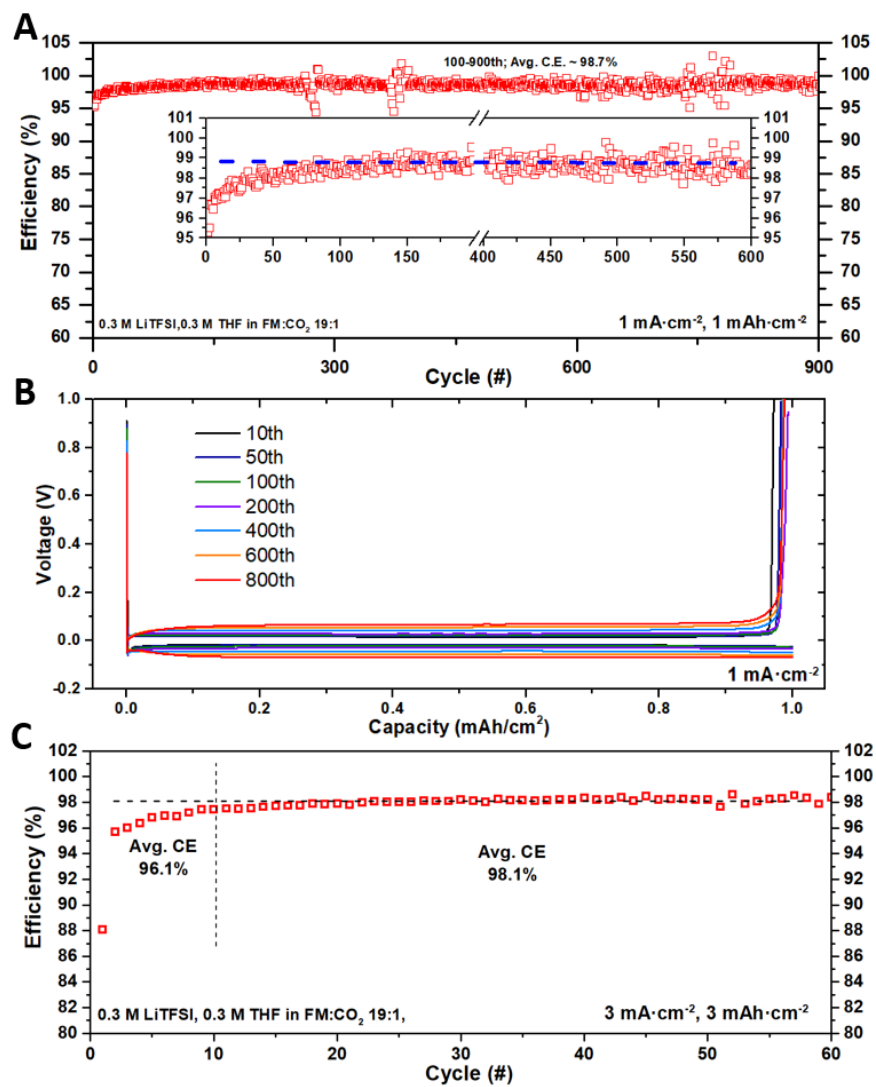
Figure S8. Electrochemical performance of Li-metal plating and stripping in the liquefied gas electrolyte. (**A**) the CE of Li plating and stripping over 900 cycles, (**B**) voltage profiles for the cell in (**A**).
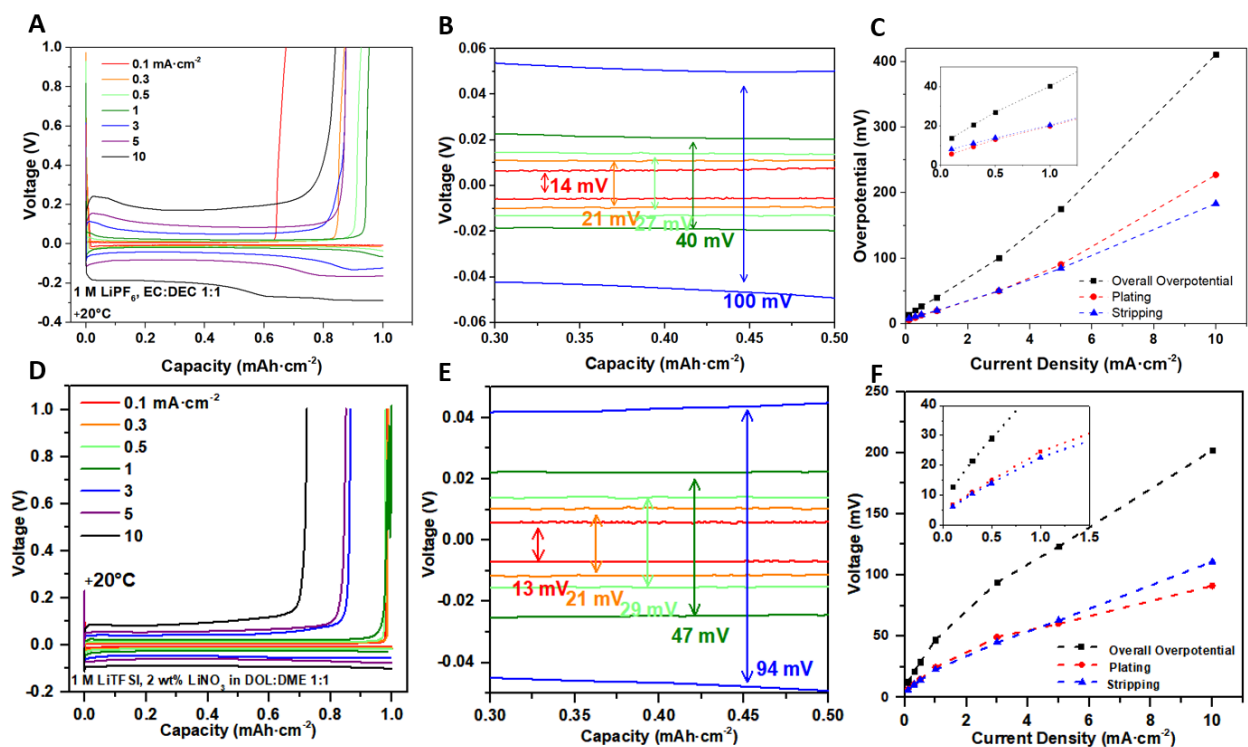
Figure S9. Electrochemical performance of Li-metal plating and stripping in the carbonate-based (**A-C**) and ether-based (**D-E**) electrolyte at +20°C at various current densities. (**A,D**) Polarization profiles, (**B,E**) enlargement of (**A,D**) in the capacity range 0.3 - 0.5 mAh·cm⁻², (**C,F**) qualitative summary of the average overpotential.
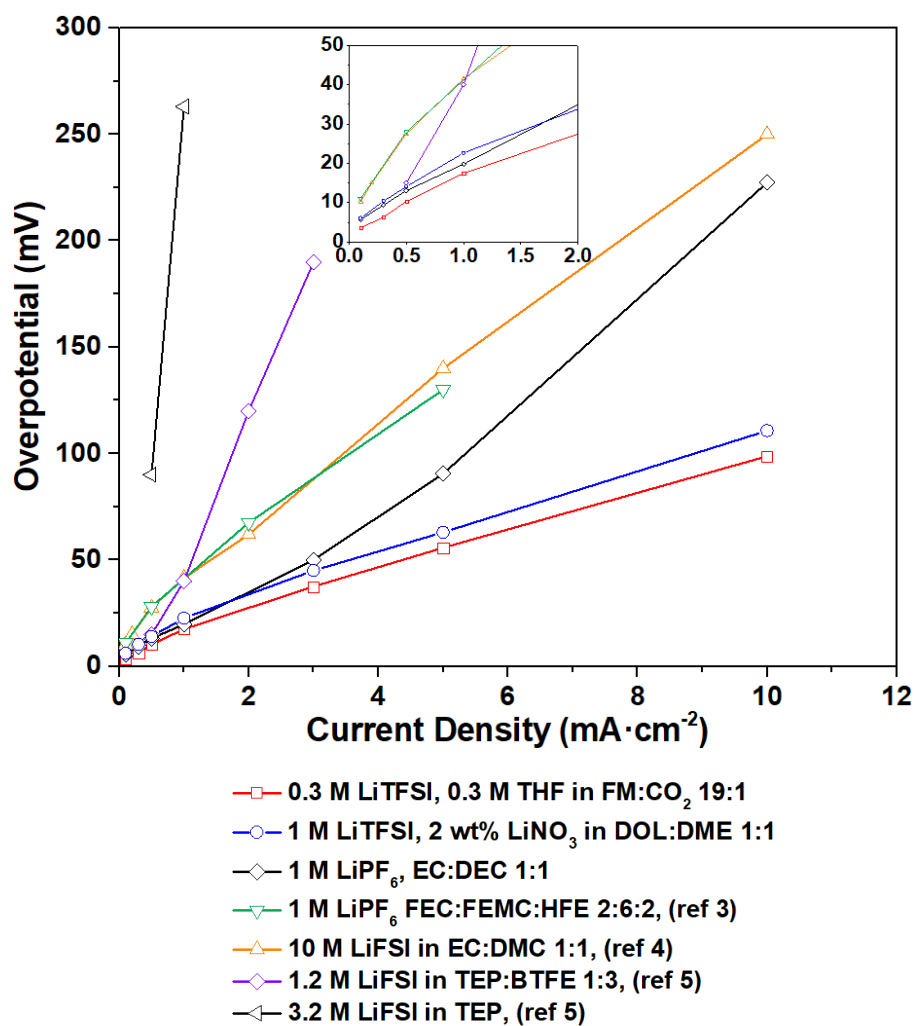
Figure S10. Polarization summary of Li-metal plating and stripping in different electrolytes[3-5] at various current densities.
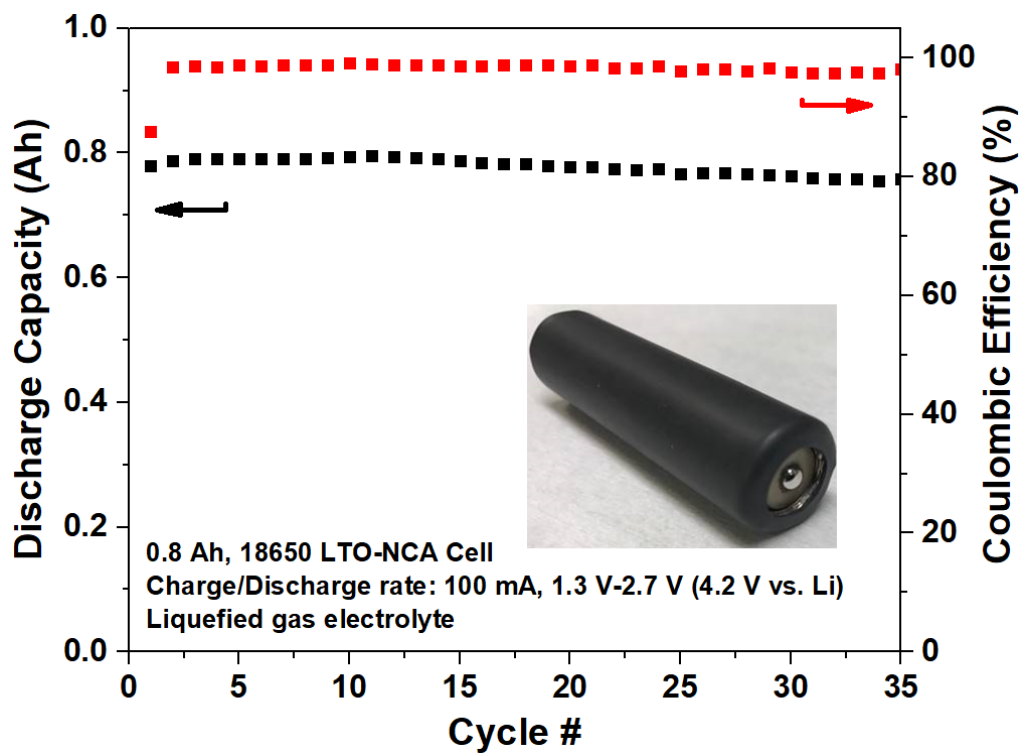
Figure S11. Demonstration of an LTO-NCA Jelly Roll in an 18650 cell format with the liquefied gas electrolyte.
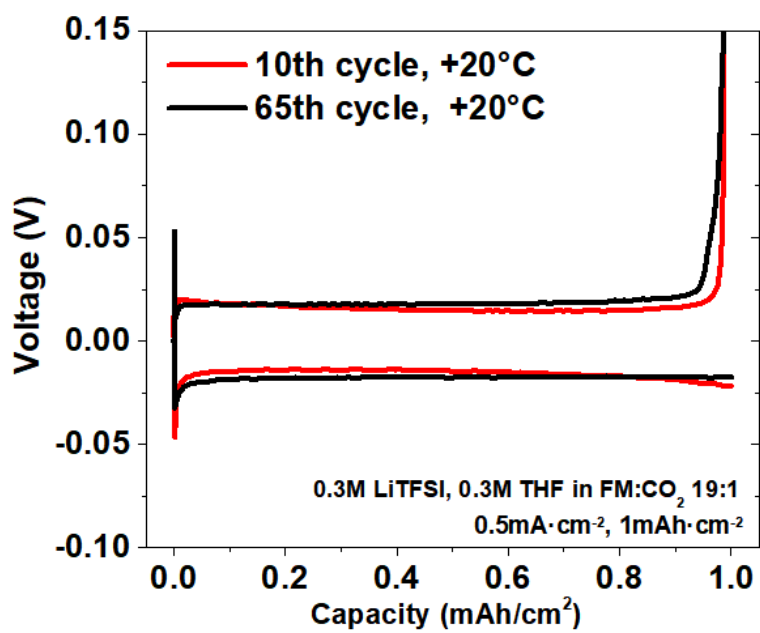
Figure S12. Li-metal plating and stripping profiles with liquefied gas electrolyte before and after the low-temperature cycling in Figure 3A.
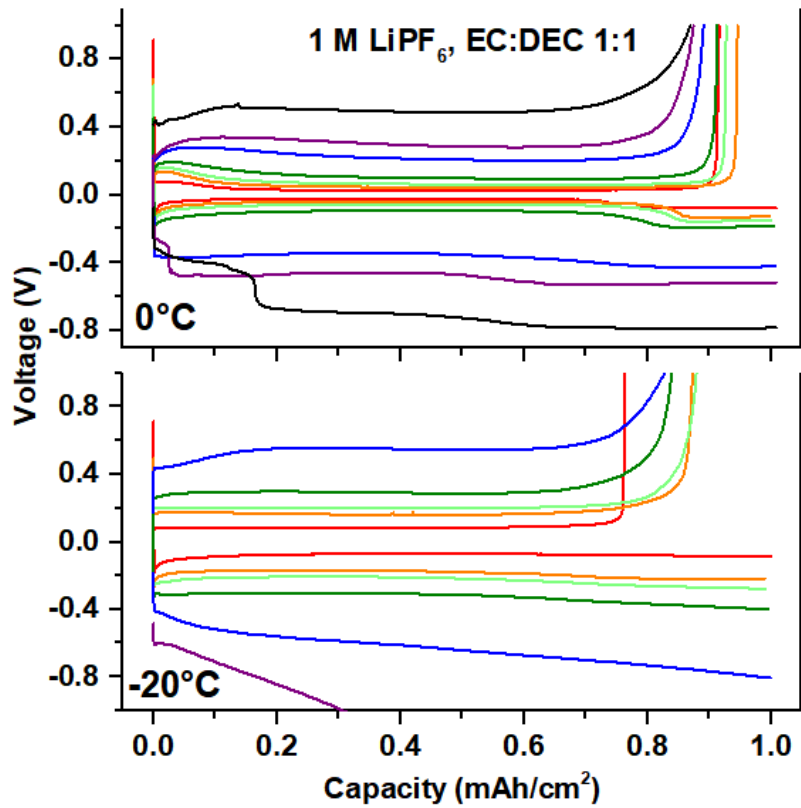
Figure S13. Polarization profiles of Li-metal plating and stripping at various current densities at 0 and -20°C in the carbonate-based electrolyte.
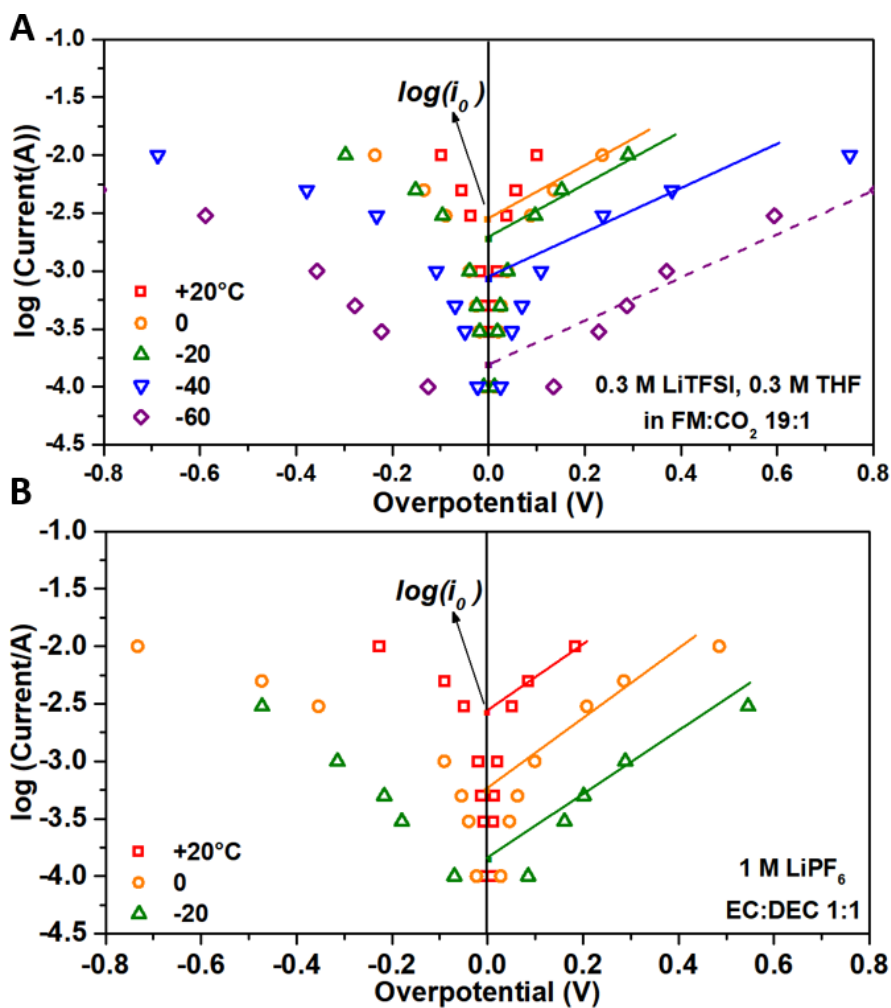
Figure S14. Tafel plot of Li-metal plating and stripping at various temperatures in different electrolytes. (**A**) 0.3 M LiTFSI, 0.3 M THF in FM:CO_2 19:1, (**B**) 1 M $LiPF_6$ in EC:DEC 1:1.

The Tafel plot was obtained by plotting overpotential versus the natural log of the Li plating and stripping current density (from Fig. 3D). The Tafel equation applies when the overpotential is over 0.1 V (or less than -0.1 V). Extrapolation of the linear region to zero overpotential provides the natural log of exchange current density (logi_0). The i_0 represents the Li plating and stripping current density in the case of no net current. Without the influence of other kinetic processes, it is an effective way to measure the rate of charge transfer reaction.

$$\eta = k \cdot (\log i - \log i_0) \qquad \text{k=Tafel Slope (Tafel Equation)}$$
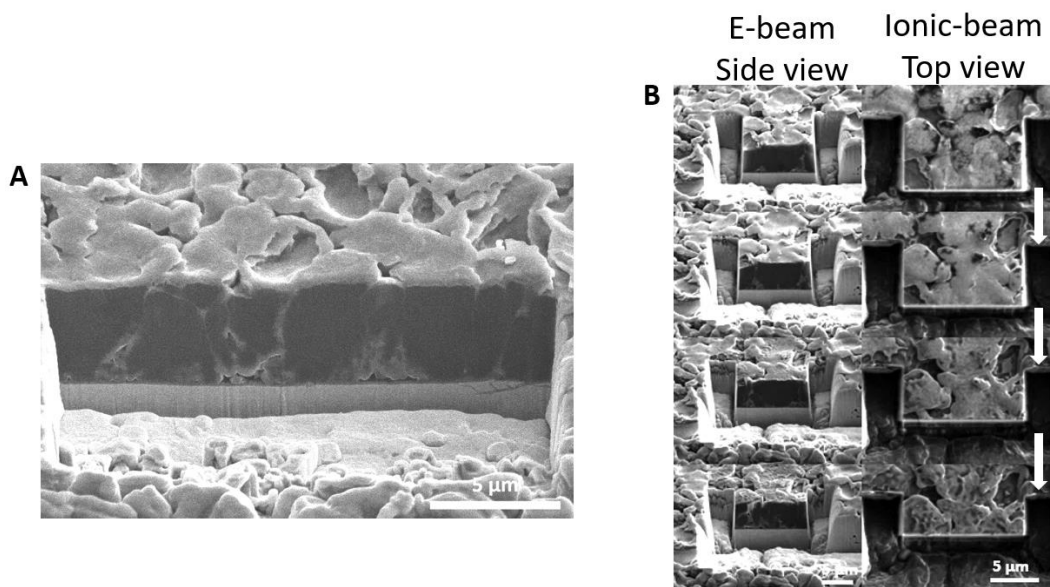
Figure S15. Cryo-FIB continuous milling process on Li-metal cross section (**A**) Regular FIB milling under cryo-condition, (**B**) cryo-FIB continuous milling process with a step space of 100 nm. 40 slices were milled with the total analysis distance of 4 µm. The e-beam image is on the left and ionic-beam image is on the right. The Li metal was electrochemically deposited at 0.5 mA·cm^{-2} with a capacity of 1 mAh·cm^{-2} on SS316L working electrode. In this example the Li metal was deposited in the liquefied gas electrolyte of 0.3 M LiTFSI, 0.3 M THF in $FM:CO_2$ 19:1.
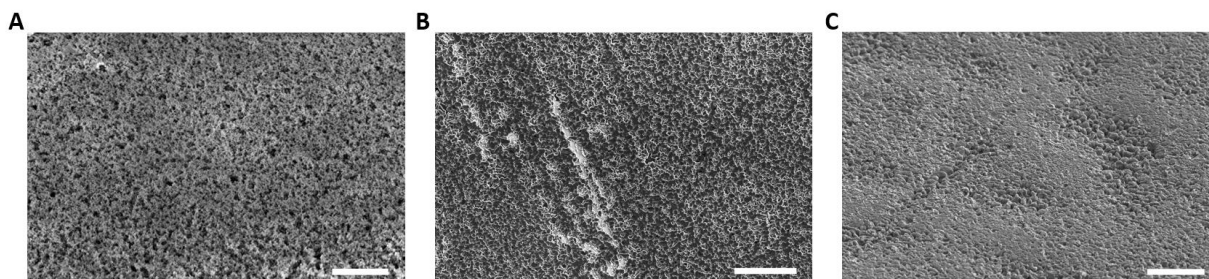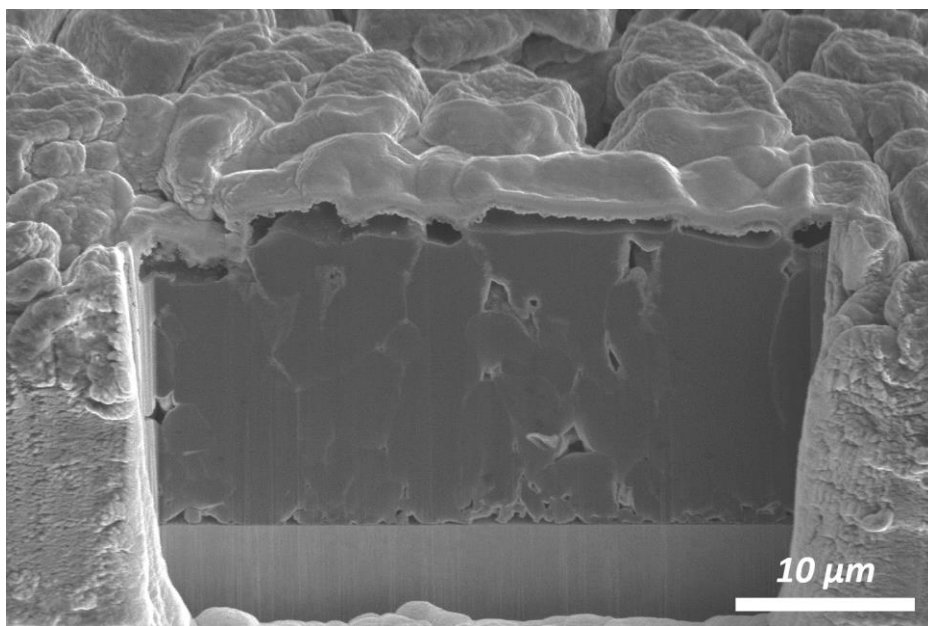
Figure S16. SEM of morphologies of plated Li in different electrolytes. (**A**) 1 M $LiPF_6$ in EC:DEC 1:1, (**B**) 1 M LiTFSI, 2 wt % $LiNO_3$ in DOL:DME 1:1, (**C**) 0.3 M LiTFSI, 0.3 M THF in FM:CO_2 19:1. The Li was plated at 0.5 mA·cm^{-2} with a capacity of 1 mAh·cm^{-2} (scale bar 30 µm).
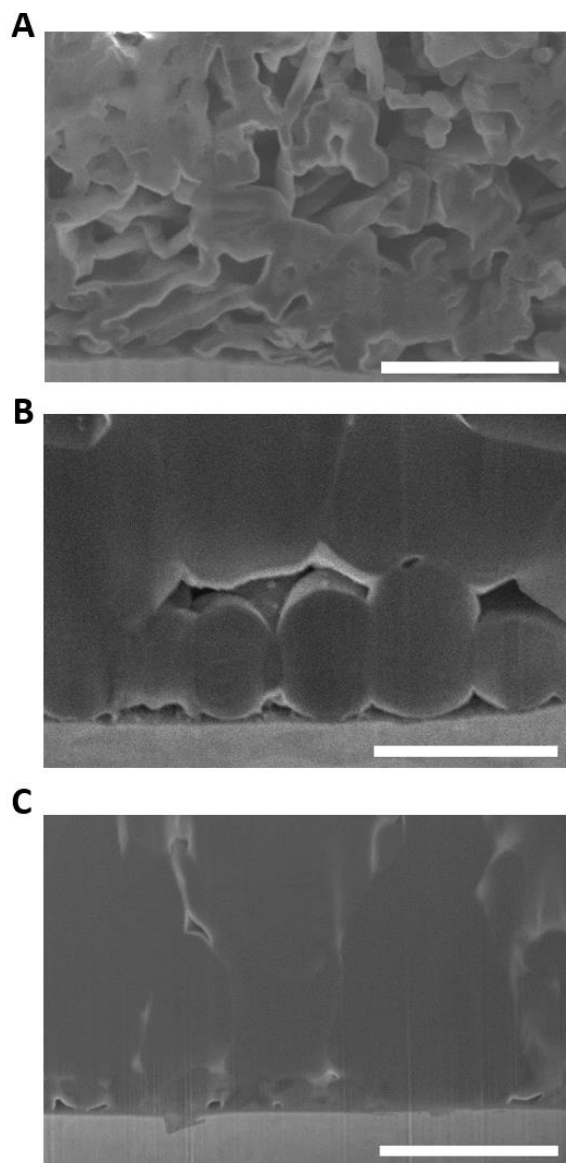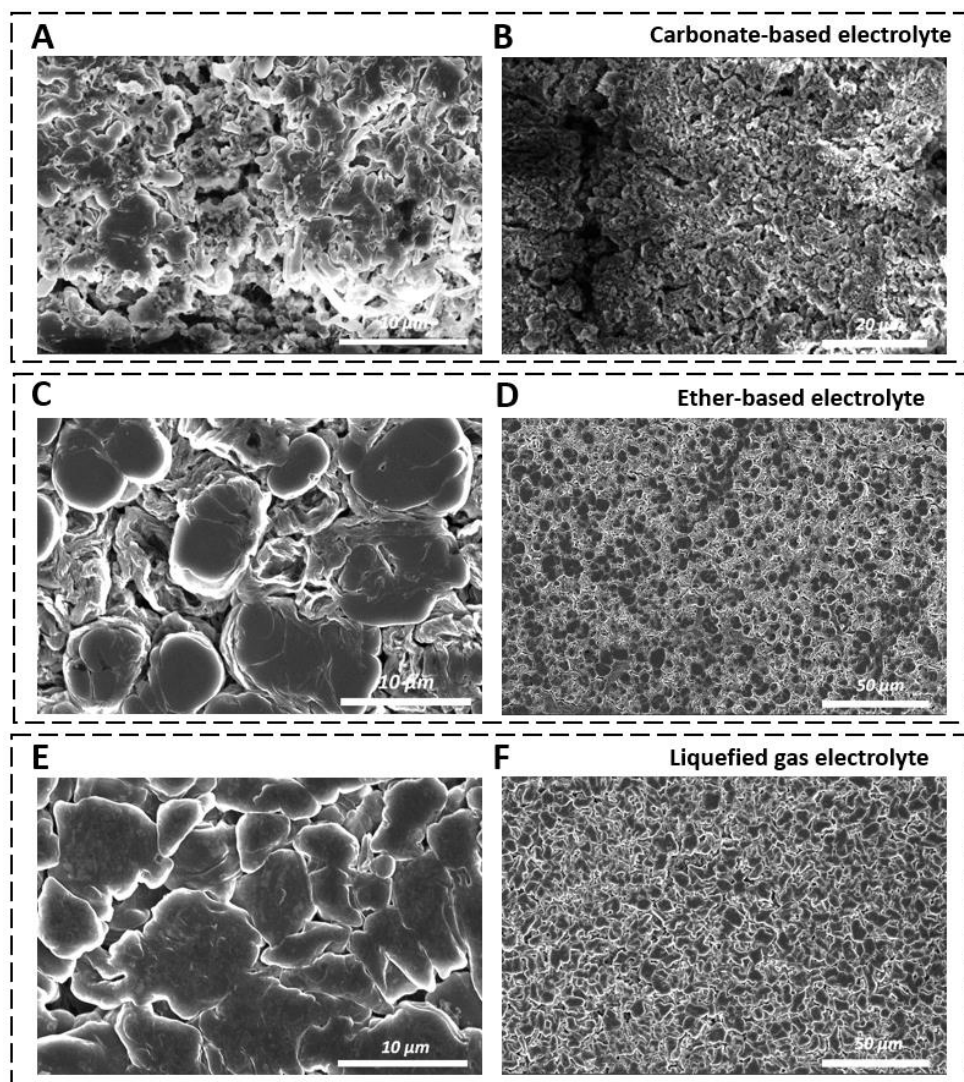
Figure S17. SEM image of morphologies of plated Li cross-sections milled by Cryo-FIB with different electrolytes. (**A**) 1 M LiPF$_6$ in EC:DEC 1:1, (**B**) 1 M LiTFSI, 2 wt % LiNO$_3$ in DOL:DME 1:1, (**C**) 0.3 M LiTFSI, 0.3 M THF in FM:CO$_2$ 19:1. The Li was plated at 0.5 mA·cm^{-2} with a capacity of 1 mAh·cm^{-2} (scale bar 2 µm).
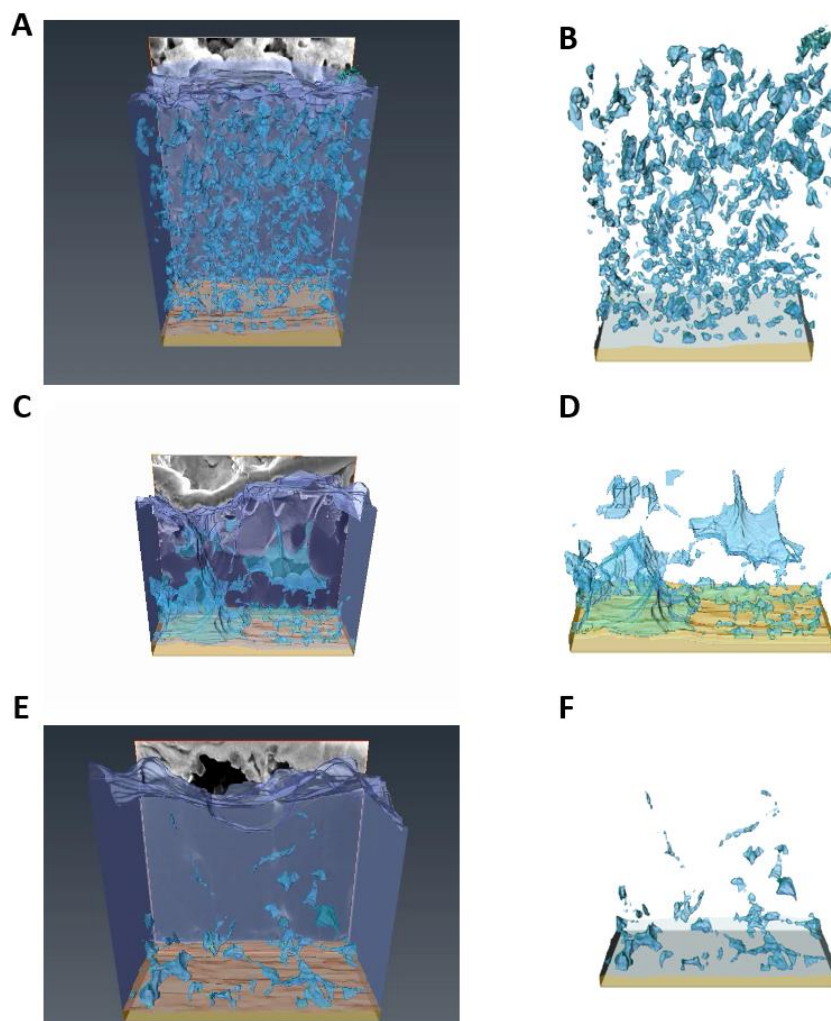
Figure S18. 3D reconstruction (**A, C, E**) and void space distribution (**B, D, F**) from cryo-FIB of deposited Li in different electrolytes. (**A, B**) 1 M $LiPF_6$ in EC:DEC 1:1, (**C, D**) 1 M LiTFSI, 2 wt % $LiNO_3$ in DOL:DME 1:1, (**E, F**) 0.3 M LiTFSI, 0.3 M THF in FM:CO_2 19:1, at 0.5 mA·cm^{-2} with a capacity of 1 mAh·cm^{-2}. Avizo Software was used for the 3D reconstruction.

**Figure S19.** Cross-sectional SEM images of 3 mAh·cm^{-2} electrochemically deposited Li via liquefied gas electrolyte. The Li metal was deposited at 0.5 mA·cm^{-2} via 0.3 M LiTFSI, 0.3 M THF in FM:CO$_2$ 19:1.

Figure S20. SEM image of plated Li-metal morphologies after 20 cycles. The Li-metal anode was cycled 20 times in different electrolytes (**A, B**) 1 M $LiPF_6$ in EC:DEC 1:1, (**C, D**) 1 M LiTFSI, 2 wt % $LiNO_3$ in DOL:DME 1:1, (**E, F**) 0.3 M LiTFSI, 0.3 M THF in $FM:CO_2$ 19:1, at 0.5 mA·cm^{-2} with a capacity of 1 mAh·cm^{-2}. The Li-metal anode was left in a lithiated state and the working electrode was left in a delithiated state.
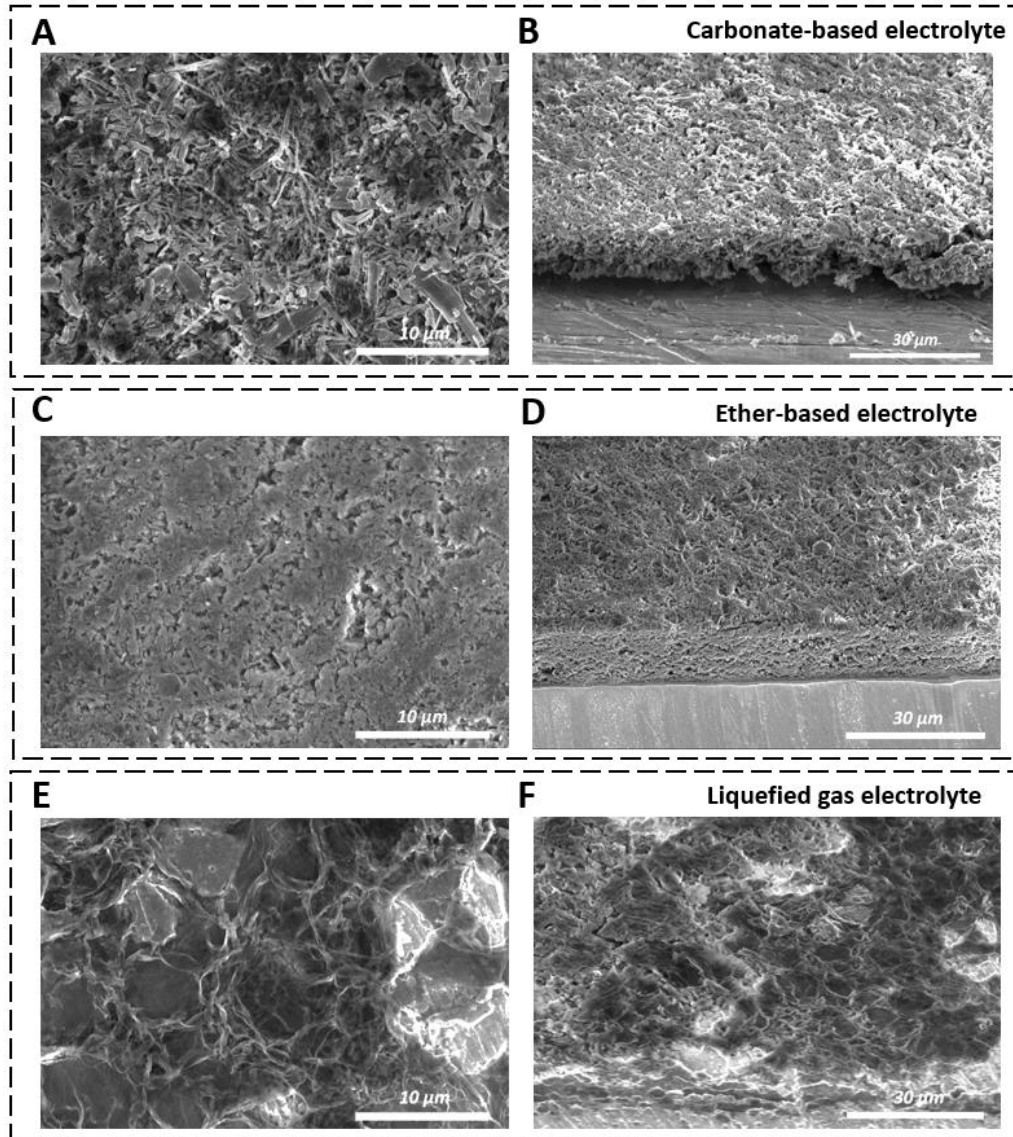
Figure S21. SEM images of stripped Li-metal morphologies after 20 cycles. The Li-metal anode was cycled 20 times in different electrolytes (**A, B**) 1 M $LiPF_6$ in EC:DEC 1:1, (**C, D**) 1 M LiTFSI, 2 wt % $LiNO_3$ in DOL:DME 1:1, (**E, F**) 0.3 M LiTFSI, 0.3 M THF in $FM:CO_2$ 19:1, at 0.5 mA·cm^{-2} with a capacity of 1 mAh·cm^{-2}. The Li-metal anode was left in a lithiated state and the working electrode was left in a delithiated state.
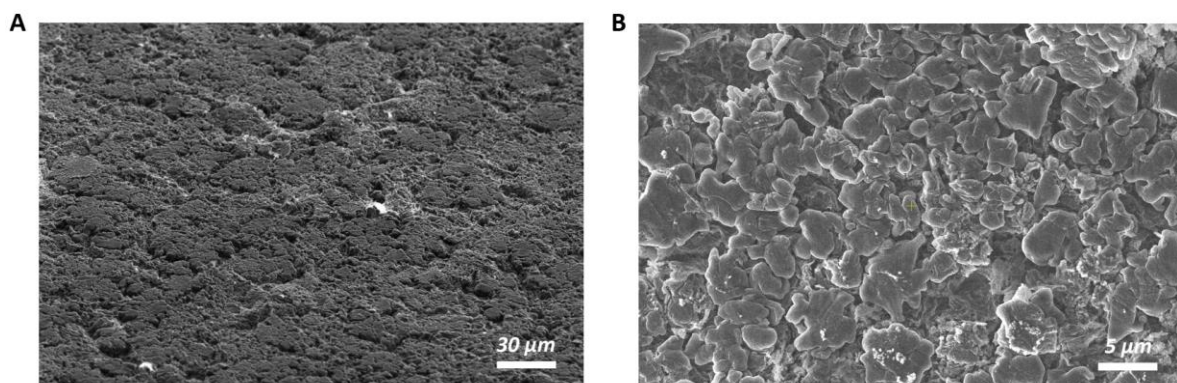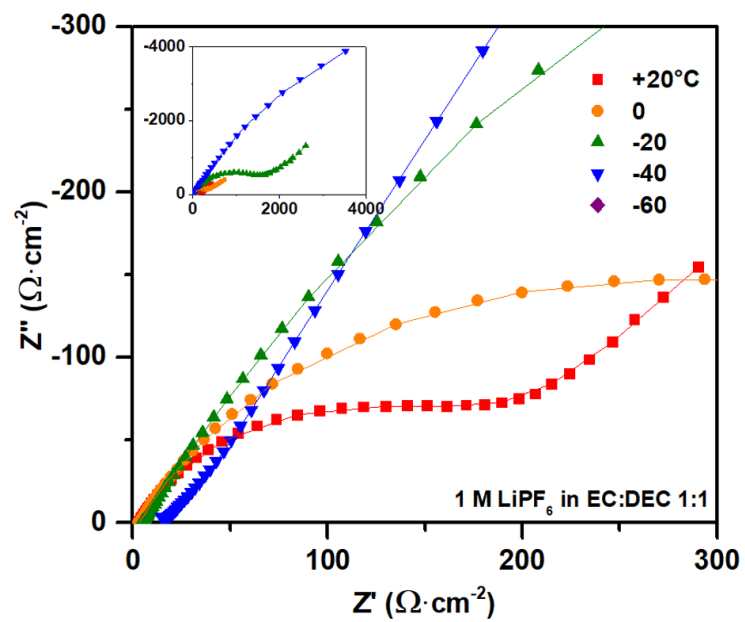
Figure S22. SEM image of plated Li-metal morphologies after 100 cycles in 0.3 M LiTFSI, 0.3 M THF in FM:CO_2 19:1, at 0.5 mA·cm^{-2} with a capacity of 1 mAh·cm^{-2}.

Figure S23. EIS impedance spectra and its fitting at various temperatures in 1 M LiPF$_6$ in EC:DEC 1:1.
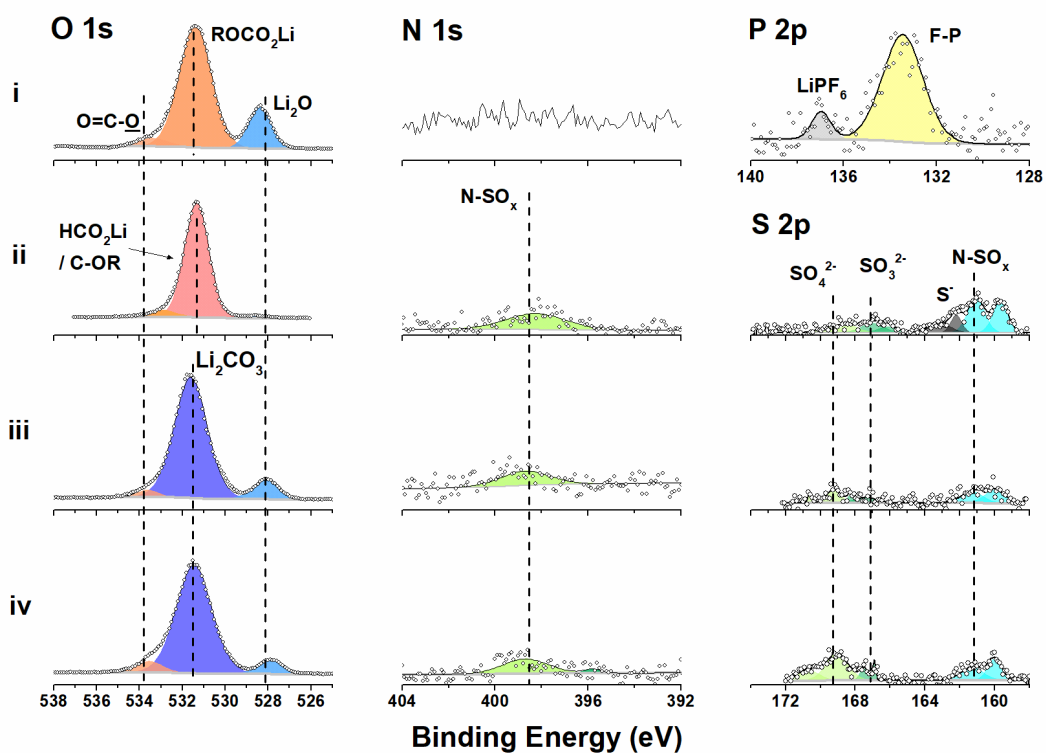
Figure S24. XPS analysis of SEI layers for the cycled Li metal in different electrolytes. **i**, 1 M LiPF$_6$ in EC:DEC 1:1, **ii**, 1 M LiTFSI, 2 wt % LiNO$_3$ in DOL:DME 1:1, **iii**, 0.2 M LiTFSI in FM:CO$_2$ 19:1, **iv**, 0.3 M LiTFSI, 0.3 M THF in FM:CO$_2$ 19:1. Li metal was cycled 20 times at a current density of 0.5 mA·cm^{-2}, with a capacity of 1 mAh·cm^{-2}.

Notes on Extracting Transport Properties from Molecular Dynamics Simulations

We followed the previously described methodology for extracting transport properties from MD simulations of electrolytes.[6]

Solvent and ion self-diffusion coefficients were extracted using the Einstein relation from linear fits to mean-square displacements divided by six as given by eq. S1

$$D_i = \frac{\lim}{t \to \infty} \frac{1}{6} \sum_i^N < ([\mathbf{R}_i(t) - \mathbf{R}_i(0)]) >^2 \tag{S1}$$

Due to the finite size of the simulation cells, long range hydrodynamic interactions across the periodic boundary of restrict the diffusion. The leading term for the finite size correction (FSC) to the self-diffusion coefficient is given by Eq. S2,[7]

$$\Delta D^{FSC} = \frac{2.837 k_B T}{6 \pi \eta L} \tag{S2}$$

where k_B is the Boltzmann constant, T is temperature, L is a linear dimension of the simulation periodic cell and η is viscosity. Solvent (FM) diffusion coefficients were corrected for the finite size using eq. S2 resulting in the increased FM self-diffusion coefficient by 4-7 % depending on temperature. Ion and co-solvent (THF) self-diffusion coefficients were increased by the same factor as FM self-diffusion coefficient. Viscosity was calculated using the Einstein relation including both diagonal and non-diagonal elements to enhance the statistics using eqs S3-S5:

$$\eta = \lim_{t \to \infty} \eta(t) = \lim_{t \to \infty} \frac{V}{20 k_B T t} \left(\left\langle \sum_{\alpha,\beta} \left(L_{\alpha\beta}(t) - L_{\alpha\beta}(0) \right)^2 \right\rangle \right) \tag{S3}$$

$$L_{\alpha\beta}(t) = \int_0^t P_{\alpha\beta}(t') \, dt' \tag{S4}$$

where k_B is the Boltzmann constant, T is temperature, t is time, V is the volume of the simulation box, P_{ab} is the stress sensor given by:

$$P_{\alpha\beta} = \frac{\sigma_{\alpha\beta} + \sigma_{\beta\alpha}}{2} - \frac{\delta_{\alpha\beta}}{3} tr(\sigma)$$

(S5)

where σ_{ab} is the stress tensor with $\delta_{ab} = 1$ for $\alpha = \beta$ and $\delta_{ab} = 0$ for $\alpha \neq \beta$.

The dynamic degree of ion uncorrelated motion (α_d) was calculated eqs. S6-S8:

$$\alpha_d = \frac{\kappa}{\kappa_{uncorr.}}$$

(S6)

$$\kappa_{uncorr} = \frac{e^2}{Vk_BT}(n_+D_+ + n_-D_-)$$

(S7)

$$\kappa = \frac{\lim}{t \to \infty} \frac{e^2}{6tVk_BT} \sum_{i,j}^{N} z_i z_j < ([\mathbf{R}_i(t) - \mathbf{R}_i(0)])([\mathbf{R}_j(t) - \mathbf{R}_j(0)]) >$$

(S8)

where e is the electron charge, V is the volume of the sample, k_B is Boltzmann's constant, T is the temperature and n_+ and n_- are the number of cations and anions, respectively. κ_{uncorr} is the "ideal" conductivity that would be realized if ion motion were uncorrelated.

Unlike calculations of viscosity and self-diffusion coefficients from MD simulations, analysis of the degree of ion uncorrelated motion (α_d) from MD simulations is not routine and deserves additional clarifications. The degree of ion uncorrelated motion (α_d) was extracted from the plateau of its time dependence following previous work[6]. A representative plot of α_d is shown in **Figure. S25**. A value of 1 would correspond to completely uncorrelated motion, while a value of zero indicates a correlated motion of cations and ions that does not contribute to change transport. **Figure S25** shows that ionic motion quickly becomes correlated on the scale of 1-100 ps leading to a plateau. At long times the curves deviate from a plateau due to higher statistical uncertainty, thus α_d is typically extracted at times less than a few percent of the simulation runs. MD simulations were performed for 70 – 130 ns, thus, α_d was extracted at time intervals of 2-3 ns. **Figure S25** clearly indicates that increasing temperature results in a systematic drop of α_d as a result of ion aggregation. Increased ionic correlation leads to a precipitous drop of conductivity as temperature approaches +40°C.

The Li$^+$ cation transference number (t_+) was extracted from MD simulations following formalism suggested by Wohde et al.[1] based upon Onsager reciprocal relations combined with linear response theory. The full matrix of charge displacements (S8) is decomposed into the contributions from cation-cation, cation-anion and anion-anion denoted as κ_{++}, κ_{+-} and κ_{--}. Note that κ_{+-} is defined using the opposite sign from Wohde et al.[1]. The transference number (t_+) is defined using two parameters α, β

$$\alpha = \kappa_{++}/(\kappa_{++} + \kappa_{--}) \text{ and } \beta = -2 \kappa_{+-}/(\kappa_{++} + \kappa_{--})$$

(S9)

$$\kappa = \kappa_{++} + \kappa_{++} + 2\,\kappa_{+-} \tag{S10}$$

$$t_+ = (\beta^2 - 4\alpha + 4\alpha^2)/(4(1-\alpha)(\beta-1)) \tag{S11}$$

As pointed out by Wohde et al.[1] parameter α (see **Figure S3A**) is similar to the transport number determined using self-diffusion coefficients, while parameter β (see **Figure S3B**) accounts for the contribution of ion correlations to t_+ (**Figure S3C**). In ideal electrolyte without any ion correlations, $\beta=0$ and $t_+=\alpha$. In the investigated electrolyte β is ~0.98 indicative of very strong ionic correlations, resulting in a significant deviation of α (self-diffusion-based transport number) from t_+.
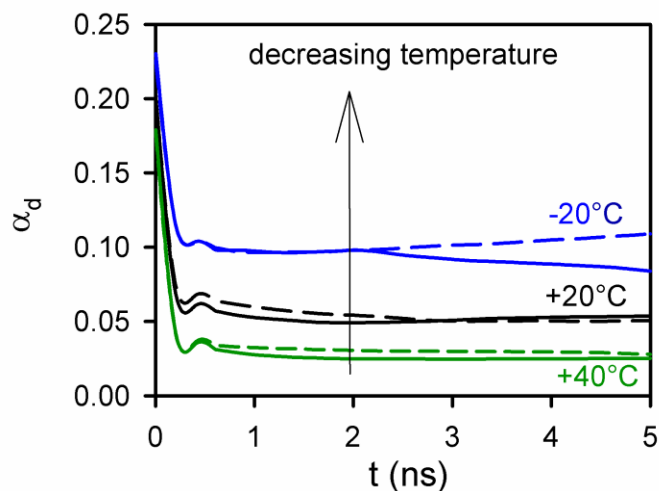
Figure S25. Representative behavior of the dynamic degree of ion uncorrelated motion (a_d) that is often called ionicity extracted from MD simulations of 0.5 M LiTFSI, 0.5 M THF in FM.

Temperature (°C)		+20	0	-20	-40	-60
Exchange current	1 M LiPF$_6$ in EC:DEC 1:1	0.00264	0.00055	0.00014	-	-
Density (i_0) (A)	0.3 M LiTFSI, 0.3 M THF in FM:CO$_2$ 19:1	0.00374	0.00301	0.00208	0.00093	0.00017

Table S1. Exchange current density of Li-metal plating and stripping at various temperatures in different electrolytes. The value is estimated from the Tafel plots (**Fig. S14**).

Electrolyte	Carbonate-based Electrolyte		Ether-based Electrolyte		Liquefied Gas Electrolyte	
Composition	1 M LiPF$_6$ in EC:DEC 1:1		1 M LiTFSI, 2 wt % LiNO$_3$ in DOL:DME 1:1		0.3 M LiTFSI, 0.3 M THF in FM:CO$_2$ 19:1	
Temperature	Impedance (ohm·cm^{-2})					
(°C)	R_e	R_{int}	R_e	R_{int}	R_e	R_{int}
+20	2.94	160.23	3.87	76.2	3.51	60.79
0	3.06	335.73	5.11	252.47	3.59	90.45
-20	4.65	1488.01	8.15	2164.08	3.90	312.48
-40	17.63	30242.05	20.34	20137.12	4.18	2844.56
-60	-	-			4.69	7248.42

Table S2. Electrochemical impedance spectroscopy fitting parameters over various temperatures. The Li-metal anode was plated/stripped 20 times at room temperature at 0.5 mA·cm^{-2} with a capacity of 1 mAh·cm^{-2}, $R_{int} = R_{int1} + R_{int2}$.

Temp (°C)	-20°C		0°C		+20°C		+20°C	
equilibration runs (ns)	82.5	112.6	90	94	61.7	80	40.1	91.7
production runs (ns)	104	131.2	115.3	112.4	107	120	78	72
D (FM) (10^{-10} m^2 s^{-1})	62	63	96	97	149	148	271	271
D (THF) (10^{-10} m^2 s^{-1})	7.6	7.6	12.7	12.0	19.7	18.9	20.8	22.1
D (TFSI$^-$) (10^{-10} m^2 s^{-1})	6.0	6.2	10.5	11.0	16.5	16.6	15.8	16.6
D (Li$^+$) (10^{-10} m^2 s^{-1})	6.2	6.3	10.6	11.0	16.7	16.4	15.7	16.4
viscosity (mPa s)	0.31	0.28	0.16	0.18	0.115	0.127	0.1	0.09

Table S3. The length of MD simulation trajectories, self-diffusion coefficients and viscosity extracted from MD simulations of 0.5 M LiTFSI, 0.5 M THF in FM.

Notes on Molecular Dynamics Simulations Code

The MD source code and input files are attached in a separate zip file (**Data S1**).

Documentation describing all MD simulation files is available at:

https://pubs.acs.org/doi/suppl/10.1021/acs.jpcc.8b05573/suppl_file/jp8b05573_si_004.pdf[8].

Supplemental References

1   Wohde, F., Balabajew, M. & Roling, B. Li+ Transference Numbers in Liquid Electrolytes Obtained by Very-Low-Frequency Impedance Spectroscopy at Variable Electrode Distances. *J. Electrochem. Soc.* **163**, A714-A721 (2016).

2   Zugmann, S. *et al.* Measurement of transference numbers for lithium ion electrolytes via four different methods, a comparative study. *Electrochimica Acta* **56**, 3926-3933 (2011).

3   Fan, X. *et al.* Non-flammable electrolyte enables Li-metal batteries with aggressive cathode chemistries. *Nature nanotechnology*, 1 (2018).

4   Fan, X. *et al.* Highly fluorinated interphases enable high-voltage Li-metal batteries. *Chem* **4**, 174-185 (2018).

5   Chen, S. *et al.* High-Efficiency Lithium Metal Batteries with Fire-Retardant Electrolytes. *Joule* (2018).

6   Borodin, O. & Smith, G. D. Quantum chemistry and molecular dynamics simulation study of dimethyl carbonate: ethylene carbonate electrolytes doped with LiPF6. *The Journal of Physical Chemistry B* **113**, 1763-1776 (2009).

7   Dunweg, B. & Kremer, K. Molecular dynamics simulation of a polymer chain in solution. *J. Chem. Phys.* **99**, 6983-6997 (1993).

8   Borodin, O. *et al.* Insights into the Structure and Transport of the Lithium, Sodium, Magnesium, and Zinc Bis (trifluoromethansulfonyl) imide Salts in Ionic Liquids. *The Journal of Physical Chemistry C* **122**, 20108-20121 (2018).